

## Stochastic modeling of plasma fluctuations with bursts and correlated noise in TCABR

M. Zurita,<sup>1</sup> W. A. Hernandez,<sup>2</sup> C. Crepaldi,<sup>1</sup> F. A. C. Pereira,<sup>3</sup> and Z. O. Guimarães-Filho<sup>1</sup>

<sup>1</sup>*Institute of Physics, University of Sao Paulo, 05508-090 Sao Paulo, Sao Paulo, Brazil*

<sup>2</sup>*Universidad Santo Tomás, Villavicencio 500003, Meta, Colombia*

<sup>3</sup>*Center for Data and Knowledge Integration for Health, Oswaldo Cruz Foundation, 41745-715 Salvador, Bahia, Brazil.*

(\*Electronic mail: [martim.zurita@usp.br](mailto:martim.zurita@usp.br))

(Dated: 12 April 2022)

Blob-like filamentary structures are omnipresent in magnetized plasmas. Their transport deteriorates the particle confinement and may damage plasma-facing components of future fusion devices. In local measurements of density, these turbulent structures are seen as high-amplitude bursts, and, since the last decade, a stochastic pulse train model (SPTM) has been developed to describe these locally measured signals. The SPTM, which is also known as a filtered Poisson process, models plasma fluctuations as a superposition of pulses plus a background with Gaussian noise. In the present article, a fitting method for this model is introduced, considering a mixture of dynamical and observational noise. The proposed method exploits the fact the model parameters can be fitted in steps, using first the signal characteristic function, then the conditionally averaged burst, and lastly the frequency spectrum. By employing this fit, we compare predictions of the model for ion saturation current measurements made with a Langmuir probe mounted in the outboard mid-plane region of the TCABR tokamak. The model is able to highlight a series of differences between the plasma edge and scrape-off layer. Furthermore, radial profiles of the SPTM parameters reveal a relation between the signal kurtosis, the intermittency of the pulses, and background parameters. Also, a linear increase in the pulse duration was found with the position. Lastly, by using recurrence quantification analysis, we show evidence that the mixture of dynamical and measurement noise may be more accurate than just one of the two to describe the dynamic behavior of density fluctuations in TCABR.

### I. INTRODUCTION

In magnetized plasmas, the confinement of particles and heat is deteriorated by the transport of blob-like filamentary structures across magnetic field lines.<sup>1–9</sup> Single point recordings of these structures capture large-amplitude bursts in the plasma edge and scrape-off layer (SOL).<sup>1,6</sup> Bursts have been studied in several plasma machines,<sup>6,8,10–14</sup> including the TCABR tokamak,<sup>15–18</sup> which is the focus of this work. In future fusion devices, the erosion rate of the main chamber wall will likely depend on the amplitude of these bursts, as well as on their duration and occurrence frequency.<sup>1,8,19,20</sup>

Over the past decade, a stochastic pulse train model (SPTM) has been developed to describe these intermittent fluctuations in local measurements of the scrape-off layer of tokamaks.<sup>21–25</sup> The SPTM consists of a superposition of pulses with randomly-distributed amplitudes and occurrence time. Predictions of the model include a Gamma probability distribution and a power-law frequency spectrum for density fluctuations.<sup>10–13,21–31</sup> The model is also referred to as a filtered Poisson process (FPP).<sup>9,24,25,28</sup>

The SPTM has been successfully applied to several low-confinement discharges in tokamaks<sup>10–13,26–31</sup> and also in a Helimak.<sup>14,32</sup> High-confinement regimes were also well described.<sup>8,9,32</sup> Furthermore, three different local measurements of density were used, with equally good results: ion saturation current,<sup>10–12,14,28–32</sup> gas puffing imaging,<sup>8,9,26–28</sup> and Lithium-Beam Emission Spectroscopy.<sup>13</sup>

Some works have considered adding a background with Gaussian noise to the SPTM, to correctly fit the density probability distribution and to account for dif-

fusivity transport.<sup>9,12–14,24,25,29,30,32</sup> In particular, a recent article analyzed the theory of two different types of noise—observational and dynamical.<sup>24</sup> The first is related to measurement error and diffusion, whereas the second is connected to the dynamics of the process. However, yet there has been no comparison between these two noise models and experimental data.

Here this gap will be fulfilled by employing the determinism from recurrence quantification analysis (RQA).<sup>33</sup> The RQA is a powerful tool to describe the structure of nonlinear signals.<sup>33–38</sup> More than just comparing the observational and dynamical noises, with the RQA analysis we will show evidence that it is actually a mixture of both processes that better describes the structure of background fluctuations in TCABR.

To do the analysis, we developed a novel fitting method for the SPTM with mixed noise. The fitting is done in steps. First, the four parameters of the probability density function (PDF) of the signal are adjusted by the characteristic function.<sup>25</sup> With the PDF parameters fixed, the characteristic duration and the asymmetry parameter of the pulses are then fitted by comparing simulated and experimental conditionally averaged bursts. Lastly, having set the PDF and pulse parameters, the noise correlation time is adjusted with the frequency spectrum. This complete description, in which seven parameters are computed, allows one to create consistent simulations and compare them with experimental data. The fitting method presented in this paper can be applied to other machines of magnetized plasmas.

Additionally, using the fitting routine, we analyzed in detail how the radial profiles of the SPTM parameters behave for a discharge in the TCABR tokamak. A positive correlation

## Physics of Plasmas

2

between the signal kurtosis, the intermittency of the pulses, and the noise parameters arose, as well as a linear increase in the pulse duration with the radial position.

About the objectives, novelties, and importance of this work, this is the first article in which (i) the SPTM is used in the TCABR tokamak; (ii) the SPTM is applied to a limited plasma (hence showing evidence of the universality of the model, which had already been applied to diverted tokamaks<sup>10–13,26–31</sup> and a Helimak<sup>14,32</sup>); (iii) a method that fits all parameters of the SPTM is introduced; (iv) a mixture of dynamical and measurement noise is proposed, indicating to be more adequate to describe plasma fluctuations; (v) the RQA determinism is applied to the SPTM (and thus adding another statistical tool to this field).

This article is organized as follows. Sec. II describes the TCABR tokamak and its experimental setup. Thereafter, Sec. III presents the stochastic pulse train model, while Sec. IV introduces the fitting method for the SPTM with mixed noise. Sec. V then applies this procedure for different positions in the TCABR tokamak. Sec. VI summarizes the results. Further details are given in Appendices A and B. The first compares analytic and numeric fits for the conditionally averaged burst, while the second stores the values and correlations obtained for the SPTM parameters.

## II. EXPERIMENTAL SETUP

The Tokamak Chauffage Alfvén Brésilien (TCABR)<sup>34,39,40</sup> has major and minor radii of  $R = 61.5$  cm and  $a = 18.0$  cm, respectively. Its plasma is circular-shaped, bounded by graphite limiters, and composed of hydrogen. Fig. 1(a) illustrates the TCABR poloidal section. The plasma current in the device is  $I_p \leq 100$  kA, having a duration of approximately 120 ms, and a period of steady regime ranging from  $T = 30$  ms to  $T = 60$  ms. The toroidal magnetic field reaches  $B_0 = 1.1$  T, while the hydrogen filling pressure is around  $3 \cdot 10^3$  Pa. In the scrape-off layer (i.e., radius  $r > a$ ), the electron density and temperature are  $n_e \approx 1.5 \cdot 10^{18}$  m<sup>-3</sup> and  $T_e \approx 5$  eV. At the core, the same quantities reach  $n_e \leq 3 \cdot 10^{19}$  m<sup>-3</sup> and  $T_e \leq 650$  eV.

This paper analyzes the discharge 34132 of TCABR, which was unperturbed and ohmically heated. The shot operated in the standard regime (L-mode) and had low magnetohydrodynamic activity, as observed with the Mirnov Coil signal (Fig. 2). During the discharge steady regime, the plasma current and line-averaged central density were  $I_p \approx 85$  kA and  $\bar{n}_e \approx 1.1 \cdot 10^{19}$  m<sup>-3</sup>, as seen in Fig. 2.

The relatively small temperature inside TCABR allows to mount probes at the plasma edge ( $0.8 < r/a < 1$ ), which is not usually possible in bigger tokamaks. In the analyzed experiment, a rake Langmuir probe was put at the outer equatorial region of the vacuum chamber. Fig. 1(b) illustrates the probe. The instrument has about 2 cm in width and height, and 8 cm in length, 5 of which are inserted inside the vacuum vessel (as depicted in Fig. 1(a)). Because of the low temperature in the TCABR SOL, interactions between the probe and the plasma are not an issue and the instrument has no relevant restrictions in obtaining time series during the whole plasma

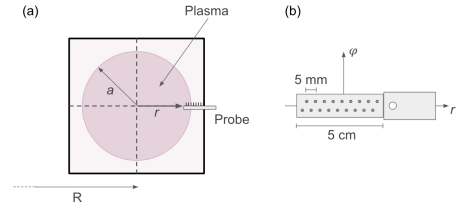


FIG. 1. (a) Scheme of the TCABR poloidal section, showing the major and minor radius ( $R = 61.5$  cm and  $a = 18.0$  cm), as well as the rake Langmuir probe. (b) Illustration of the rake probe, with tips perpendicular to the radial-toroidal plane.

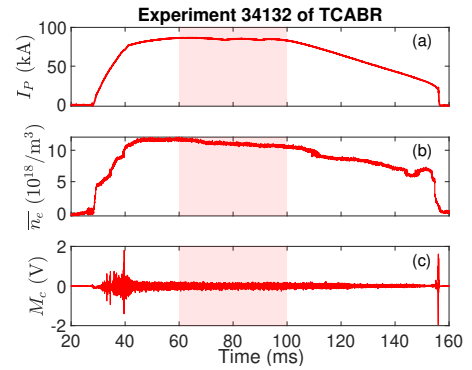


FIG. 2. Main plasma characteristics of the TCABR experiment 34132: (a) Plasma current; (b) Line-averaged electron density; (c) Mirnov coil signal. The highlighted area corresponds to the interval chosen for the analysis.

discharge. The probe has 18 pins, divided into two rows. In the analyzed experiment, eight tips of a single row were set to measure ion saturation current, proportional to the plasma density.<sup>29</sup> The used pins were separated by 5 mm each, in the radial direction. The most inward tip was set at  $r = 17.0$  cm, that is, 1.0 cm inside the plasma edge. Further details about the rake probe and the experimental setup used here are given in Ref. 40.

The interval between measurements was  $\Delta t = 0.5$   $\mu$ s. The analysis was performed between  $t_i = 60$  ms and  $t_f = 100$  ms, when the plasma was approximately steady (as seen in Fig. 2). Thus, the duration of the analysis was  $T = 40$  ms, corresponding to  $N_{pt} = T/\Delta t = 8 \cdot 10^4$  points of saturation current for each position.

## III. STOCHASTIC PULSE TRAIN MODEL

The stochastic pulse train model,<sup>21–25</sup> usually referred to as a filtered Poisson process,<sup>9,24,25,28</sup> or as a shot noise

process,<sup>21,24,25</sup> consists of a superposition of pulses with random amplitudes and occurrence times. It models turbulent density fluctuations in single-point recordings of magnetically confined plasmas. Often, a background with Gaussian-distributed fluctuations is added to account for measurement error, diffusive transport, and plasma equilibrium, improving the quality of experimental PDF fit<sup>9,13,14,27</sup>. The saturation current is thus modeled as a background,  $I_b(t)$ , plus a train of pulses,  $I_p(t)$ , from which bursts arise:

$$I_{sat}(t) = I_b(t) + I_p(t). \quad (1)$$

The pulse train models turbulent fluctuations and is given by

$$I_p(t) = \sum_{j=1}^{N_p} A_j \phi\left(\frac{t-t_j}{\tau_d}; \lambda\right), \quad (2)$$

where  $N_p$  is the number of pulses created in the analyzed interval and  $A_j$  and  $t_j$  are the amplitude and time occurrence of the  $j$ -th pulse.  $\tau_d$  and  $\lambda$  are respectively the characteristic duration and the asymmetry parameter of the pulses. Recent works have shown that, for a given experiment and a fixed position, bursts with different amplitudes have a similar duration and asymmetry.<sup>10,11,26</sup> Also, in this model  $\tau_d$  and  $\lambda$  do not interfere in the distribution of  $I_p(t)$ .<sup>23</sup> For these reasons, these two parameters are presumed constant for all pulses. In addition, all parameters of Eq. (2) are supposed independent of each other.<sup>23</sup>

Following Fig. 3 and vast experimental evidence gathered on distributions of bursts,<sup>8-14,28</sup> it is inferred that the pulse amplitude  $A_j$  is given by an exponential distribution,

$$P_A(A_j) = \frac{1}{\langle A \rangle} \exp\left(-\frac{A_j}{\langle A \rangle}\right). \quad (3)$$

(Throughout this paper,  $\langle \cdot \rangle$  indicates the mean of a distribution.) Provided with the same references, the occurrence time  $t_j$  of the pulses is supposed uncorrelated and uniformly distributed (uncorrelated bursts),

$$P_t(t_j) = 1/T \quad \forall j, \quad (4)$$

where  $T$  is the interval of the analyzed signal.

The distributions of occurrence time  $P_t$ , waiting time between pulses  $P_w$ , and number of pulses  $N_p$  are intrinsically related (see for example p. 135 and p. 140 of Ref. 41). As the occurrence times  $t_j$  are uncorrelated and uniform, it results that  $\Delta t_w$  and  $N_p$  are exponentially and Poisson distributed, respectively. This justifies referring to the model as a Poisson process.<sup>9</sup> Here we approximate  $N_p$  as being the expected value of its own distribution, aiming to decrease statistical fluctuations in the simulations without losing important features of the model.

The last term to name in Eq. (2) is the pulse shape  $\phi$ , given by a two-sided exponential

$$\phi(s; \lambda) = \begin{cases} \exp(s/\lambda), & s < 0. \\ \exp[-s/(1-\lambda)], & s \geq 0. \end{cases} \quad (5)$$

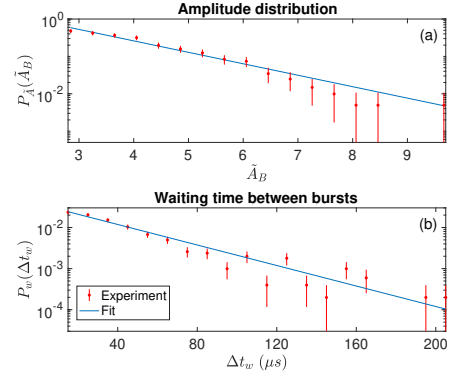


FIG. 3. Burst distributions of (a) amplitude and (b) waiting time between events for the position  $r = 18.5$  cm. The PDFs were fitted by exponentials. The bursts were detected using the formalism of conditional averaging, i.e., one pulse was identified as a burst if its peak was higher than the average of the signal in at least 2.5 standard deviations.<sup>6,11</sup> The number of extreme events detected in 40 ms was 559, as shown in Fig. 12. The signal was normalized by Eq. (22). The uncertainties were obtained by assuming that each histogram bar followed a Poisson distribution ( $\sigma_{P_j} \propto \sqrt{P_j}$ ).

$\phi$  is inspired by the conditionally averaged burst.<sup>6,21,27</sup>

An important quantity is the so-called intermittency parameter,<sup>11,12,22-25,27-29,31</sup>

$$\gamma = \tau_d \frac{N_p}{T} = \frac{\tau_d}{\tau_w}, \quad (6)$$

where  $\tau_w = T/N_p$  is the average waiting time between pulses.  $\gamma$  increases with the pulse overlap, while  $\gamma^{-1}$  increases with the intermittency level.<sup>21,22</sup>

With all this information gathered about the train of pulses,  $I_p(t)$ , results that its PDF is given by a Gamma distribution with scale parameter  $\langle A \rangle$  (average amplitude of the pulses) and shape parameter  $\gamma = \tau_d/\tau_w$ .<sup>21,25</sup>

$$P_p(I_p(t)) = \frac{1}{\langle A \rangle \Gamma(\gamma)} \left(\frac{I_p(t)}{\langle A \rangle}\right)^{\gamma-1} \exp\left(-\frac{I_p(t)}{\langle A \rangle}\right). \quad (7)$$

Furthermore, the background term of Eq. (1) has PDF

$$P_b(I_b(t)) = \frac{1}{\sqrt{2\pi}\sigma_N^2} \exp\left[-\frac{(I_b(t)-I_0)^2}{2\sigma_N^2}\right]. \quad (8)$$

The constant  $I_0$  accounts for the equilibrium background plasma. In its turn,  $\sigma_N$  is the standard deviation of the Gaussian noise and it can correspond to diffusive fluctuations, observational noise, or dynamical noise.<sup>14,24</sup> Observational noise is related to the error in the system due to imprecision in measurement. Dynamical noise, on the other hand, is related to the dynamics of the stochastic process.<sup>24</sup>

This train of pulses plus a Gaussian background has mean, standard deviation, skewness, and kurtosis given by<sup>9,24</sup>

$$\langle I_{sat} \rangle = \gamma \langle A \rangle + I_0, \quad (9a)$$

$$\sigma_I^2 = \gamma \langle A \rangle^2 (1 + \varepsilon), \quad (9b)$$

$$S_I = \frac{2}{\gamma^{1/2} (1 + \varepsilon)^{3/2}}, \quad (9c)$$

$$K_I = 3 + \frac{6}{\gamma^2 (1 + \varepsilon)^2}, \quad (9d)$$

where the pulse contributions for the average and variance are  $\langle I_p \rangle = \gamma \langle A \rangle$  and  $\sigma_p^2 = \gamma \langle A \rangle^2$  and  $\varepsilon = \sigma_{\mathcal{N}}^2 / \sigma_p^2$  is called the noise parameter.<sup>24</sup>

Moreover, the resulting PDF from the convolution of Eqs. (7) and (8) is rather intricate (Eq. (A6) of Ref. 24). Thus, it is preferable to fit the characteristic function (CF), as proposed in Ref. 25. The CF holds the same information as the PDF, as they are Fourier transforms of each other,<sup>42</sup>

$$C_I(u) = \int_{-\infty}^{\infty} e^{iul} P_I(l) dl, \quad (10)$$

where  $l$  is the random variable with PDF  $P_I(l)$ ,  $u \in \mathbb{R}$  is the CF variable, and  $i = \sqrt{-1}$  is the imaginary unit. (For more details about CFs see for example Chap. 4. of Ref. 42.) The characteristic functions of the Gamma and the normal distributions are respectively

$$C_p(u) = (1 - i \langle A \rangle u)^{-\gamma} \quad (11)$$

and

$$C_b(u) = \exp\left(i l_0 u - \frac{1}{2} \sigma_{\mathcal{N}}^2 u^2\right). \quad (12)$$

Also, the characteristic function of a sum of independent random variables is the product of their individual CFs. Thus, the characteristic function of  $I_{sat} = I_p + I_b$  is simply

$$C_I(u) = (1 - i \langle A \rangle u)^{-\gamma} \exp\left(i l_0 u - \frac{1}{2} \sigma_{\mathcal{N}}^2 u^2\right). \quad (13)$$

Eq. (13) will be used in Sec. IV to fit  $\gamma$ ,  $\langle A \rangle$ ,  $I_0$ , and  $\sigma_{\mathcal{N}}$ .

Inspired by Ref. 24, in this paper we will compare dynamical noise with observational noise. The first is correlated, but the noise correlation does not alter the PDF.<sup>24,25</sup>

Dynamical noise is a type of Ornstein-Uhlenbeck (OU) process, which can be defined by the equation<sup>43-45</sup>

$$X(t + dt) = X(t) - \frac{1}{\tau_{\mathcal{N}}} X(t) dt + c^{1/2} g(t) (dt)^{1/2}. \quad (14)$$

$\tau_{\mathcal{N}}$  is called the relaxation or correlation time of the OU noise.<sup>43,44</sup> For the case of dynamical noise, the background fluctuations are associated with the dynamics of the main pulses, in such a way that the correlation time is equal to the pulse characteristic duration,  $\tau_{\mathcal{N}} = \tau_d$ .<sup>24</sup>

Following Ref. 43,  $c$  in Eq. (14) is the diffusion coefficient and  $dt$  is a "positive infinitesimal", that is, a real variable confined in the interval  $[0, \delta]$ , with  $\delta \rightarrow 0$ .  $g(t)$  is a temporally

uncorrelated Gaussian variable with mean 0 and variance 1. For a given initial condition  $X(t_0) = x_0$  the average and variance of the OU process are

$$\langle X(t) \rangle = x_0 e^{-(t-t_0)/\tau_{\mathcal{N}}}, \quad (15a)$$

$$\sigma_X^2 = \frac{1}{2} c \tau_{\mathcal{N}} \left[ 1 - e^{-2(t-t_0)/\tau_{\mathcal{N}}} \right]. \quad (15b)$$

For our purposes, the process can be considered stationary, because very rapidly in the analyzed signals  $e^{-(t-t_0)/\tau_d} \rightarrow 0$ . Synthetic realizations of the OU process can be easily implemented with Gillespie's algorithm (Eq. (1.10) of Ref. 43).

The correlation time  $\tau_{\mathcal{N}}$  is the interval in which the autocorrelation function of  $X(t)$  decays by a factor of  $e$  (see for example Eq. (B16) of Ref. 24),

$$R_X(\tau) = \sigma_X^2 \exp\left(-\frac{|\tau|}{\tau_{\mathcal{N}}}\right). \quad (16)$$

Consequently, the power spectral density of the OU process is Lorentzian (Eq. (B15) of Ref. 24),

$$\Omega_X(\omega) = \frac{2\tau_{\mathcal{N}}\sigma_X^2}{1 + \tau_{\mathcal{N}}^2\omega^2}. \quad (17)$$

In this work, we propose that the background fluctuations are composed at the same time by dynamical noise (related to the system dynamics) and observational noise (related to measurement error). As it will be shown in Subsec. VB, this noise mixture will be important to approximate the RQA determinism of synthetic signals to experimental ones. It also is physically expected that, in general, the signal has at the same time measurement and dynamical noise. Mathematically, the expression for the background of Eq. (1) and (8) then becomes

$$I_b(t) = I_0 + I_D(t) + I_O(t), \quad (18)$$

where  $I_D(t)$  is the dynamical noise, that is, a OU process with correlation time  $\tau_{\mathcal{N}} = \tau_d$ , vanishing mean, and variance  $\sigma_D^2$ . In its turn,  $I_O(t)$  corresponds to observational (or measurement) noise, that is, uncorrelated Gaussian noise (which can be regarded as an OU process with  $\tau_{\mathcal{N}} \rightarrow 0$ ) with null average and variance  $\sigma_O^2$ . The noise variances are connected to the total variance of Eq. (8) by

$$\sigma_{\mathcal{N}}^2 = \sigma_D^2 + \sigma_O^2. \quad (19)$$

It is thus interesting to define a parameter of balance between dynamical and observational noise,

$$\lambda_{\mathcal{N}} = \left(\frac{\sigma_D}{\sigma_{\mathcal{N}}}\right)^2, \quad (20)$$

such that  $\sigma_D^2 = \lambda_{\mathcal{N}} \sigma_{\mathcal{N}}^2$  and  $\sigma_O^2 = (1 - \lambda_{\mathcal{N}}) \sigma_{\mathcal{N}}^2$ .

Following Eq. (C8) of Ref. 23 and Eq. (17) of Ref. 24, the PSD of  $I_{sat} = I_p + I_b$  is

$$\Omega_I(\omega) = \frac{2\tau_d\sigma_p^2}{(1 + \tau_d^2\omega^2)(1 + \tau_{\mathcal{N}}^2\omega^2)} + \frac{2\tau_d\lambda_{\mathcal{N}}\sigma_{\mathcal{N}}^2}{1 + \tau_d^2\omega^2} + \Delta t (1 - \lambda_{\mathcal{N}}) \sigma_{\mathcal{N}}^2 + 2\pi\delta(\omega) (I_{sat})^2. \quad (21)$$

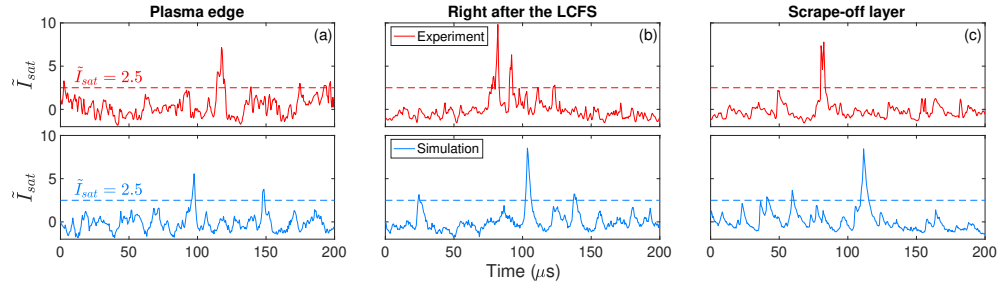


FIG. 4. The top panels show, in red, excerpts of time series of  $\bar{I}_{sat}$  for three positions: (a) plasma edge ( $r = 17.0$  cm), (b) right after the last closed flux surface ( $r = 18.5$  cm) and (c) in the scrape-off layer ( $r = 19.5$  cm). The bottom panels show, in blue, simulations from the SPTM.

The first, second, and third terms on the right correspond respectively to  $I_p$ ,  $I_D$ , and  $I_C$ . Furthermore,  $\tau_r = \lambda \tau_d$  and  $\tau_f = (1 - \lambda) \tau_d$  are respectively the characteristic duration of the pulse rise and fall,  $\Delta t$  is the interval between measurements (equal to  $0.5 \mu\text{s}$  in TCABR), and  $\delta(\omega)$  is the Dirac distribution. In Subsec. IV C, the power spectrum will be used to fit the noise-balance parameter  $\lambda_{\mathcal{N}}$ .

In Fig. 4, the red curves show  $200 \mu\text{s}$  of experimental saturation current for three positions in TCABR. In blue, are depicted synthetic realizations of the pulse train model with mixed noise. Sec. IV and V will explain how we obtained the parameters for these simulations. Following the standard procedure,<sup>10–12,14,30,31</sup> the signal has been normalized to

$$\bar{I}_{sat} = \frac{I_{sat} - \langle I_{sat} \rangle}{\sigma_I}, \quad (22)$$

such that  $\bar{I}_{sat}$  has a zero mean and unit standard deviation. In each panel of Fig. 4, large-amplitude bursts stand out, with a peak higher than the average  $\bar{I}_{sat} = 0$  in several standard deviations. The dashed line  $\bar{I}_{sat} = 2.5$  demarcates the threshold for bursts detection.

#### IV. FITTING METHOD

The pulse train model with mixed noise has seven parameters to be adjusted (Table I). For them, we propose a "pyramidal" fitting method. First, the characteristic function is adjusted, taking advantage of the fact that it depends solely on the distribution parameters  $\gamma$ ,  $\langle A \rangle$ ,  $I_0$ , and  $\sigma_{\mathcal{N}}$  (Eq. (13)). With this, the pyramid basis is established. Having fixated these last four, the conditional average of bursts (CAB),  $\phi_B$ , can be fitted with simulations to obtain the pulse parameters  $\tau_d$  and  $\lambda$ .  $\phi_B$  does not depend on the noise balance  $\lambda_{\mathcal{N}}$  as this last is a background variable, not interfering with extreme events such as bursts.  $\tau_d$  and  $\lambda$  form the middle of the pyramid. Finally, having fixated six parameters, the percentage of dynamical noise,  $\lambda_{\mathcal{N}}$ , can be adjusted by the power spectral density. In the following subsections, the fitting method will be detailed and applied to position  $r = 19.5$  cm of TCABR.

#### A. Fit of the characteristic function

The characteristic function of the pulse train model with Gaussian noise is given by Eq. (13). To estimate the CF from a discrete signal  $I = (I_1, I_2, \dots, I_{N_{pt}})$ , the empirical characteristic function (ECF) is used,<sup>25,46</sup>

$$C_I(u) = \frac{1}{N_{pt}} \sum_{j=1}^{N_{pt}} e^{iuI_j}. \quad (23)$$

To fit the CF, we note that  $C_I(u)$  and  $C_I(-u)$  carry the same information, since  $C_I(u) = C_I(-u)$ . Hence, we can define a function equivalent to  $C_I(u)$  that allocates the real part of  $C_I(u)$  in negative values of  $u$ , and lets the imaginary part be in  $u > 0$ ,

$$C_I(u) \equiv \begin{cases} \text{Re } C_I(u), & u \leq 0, \\ \text{Im } C_I(u), & u > 0. \end{cases} \quad (24)$$

$C_I(u)$  is given by Eq. (13). Since  $C_I(u)$  is not complex, one can use it to fit the parameters  $\gamma$ ,  $\langle A \rangle$ ,  $I_0$ , and  $\sigma_{\mathcal{N}}$  with a Levenberg–Marquardt least-squares method (see for example Appendix B of Ref. 17, or Sec. 8.1, 8.2, and 8.4–8.6 of Ref. 47). Fig. 5(a) shows a fit of  $C_I(u)$ , whose covariance matrix was estimated with repeated simulations with fixed parameters.

Characteristic functions can have points with non-negligible correlation, as evidenced by the regions near the diagonals of the correlation matrix in Fig. 5(b). Because of

TABLE I. Parameters adjusted by the CF-CAB-PSD fit.

| Symbol                  | Name                          | Eq.  | Fitted by |
|-------------------------|-------------------------------|------|-----------|
| $\gamma$                | Intermittency parameter       | (6)  | CF        |
| $\langle A \rangle$     | Mean amplitude of the pulses  | (3)  | CF        |
| $I_0$                   | Equilibrium background plasma | (8)  | CF        |
| $\sigma_{\mathcal{N}}$  | Noise standard deviation      | (8)  | CF        |
| $\tau_d$                | Pulse characteristic duration | (2)  | CAB       |
| $\lambda$               | Pulse asymmetry parameter     | (5)  | CAB       |
| $\lambda_{\mathcal{N}}$ | Noise-balance parameter       | (20) | PSD       |

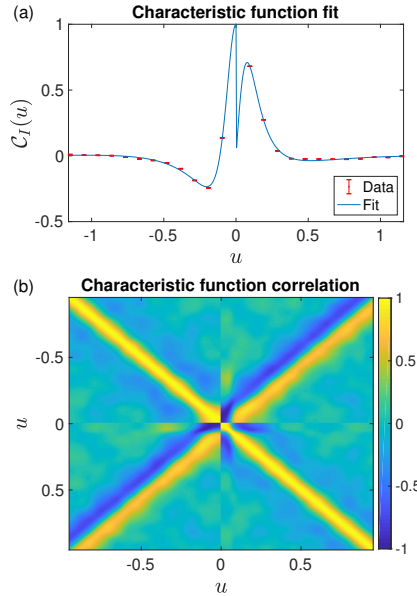


FIG. 5. Fit of  $C_I(u)$  (a) and its correlation matrix in high resolution (b) for the position  $r = 19.5$  cm. The uncertainties in  $C_I(u)$  were estimated with repeated simulations with fixed parameters.

this, it is crucial to use few points  $u$  in the fit, as otherwise, a highly correlated ECF can lead to a non-invertible covariance matrix (i.e. with determinant 0), which would preclude the use of a least-squares method. The chosen array of  $u$  was

$$\vec{u} = \frac{u_{1\%}}{12} (1, 2, \dots, 12), \quad (25)$$

where  $u_{1\%}$  is the smallest positive value such that  $|C_I(u_{1\%})| = 1\%$ . For  $C_I(u)$  (Eq. (24)), the effective array was composed of  $-\vec{u}$  and  $\vec{u}$ . The point  $u = 0$  is not fitted since by definition  $C_I(0) = 1$  (Eq. (10)) and, consequently,  $C_I(0)$  has a null variance.

### B. Fitting the CAB with simulations

Having fixed the parameters  $\gamma$ ,  $\langle A \rangle$ ,  $I_0$ , and  $\sigma_N$  by the CF fit (Subsec. IV A), it is now possible to evaluate the characteristic duration  $\tau_d$  and the asymmetry parameter  $\lambda$  of the pulses with the conditional average of bursts. Following the usual routine,<sup>10–13,26,27,30,31</sup> bursts are identified in the saturation current as peaks with amplitude higher than the signal average by at least 2.5 standard deviations:  $I_{sat} > \langle I_{sat} \rangle + 2.5\sigma_I$ . The detected bursts are put in a time axis with each peak at  $t = 0$ . The average of them is then performed to obtain the conditionally averaged burst waveform.

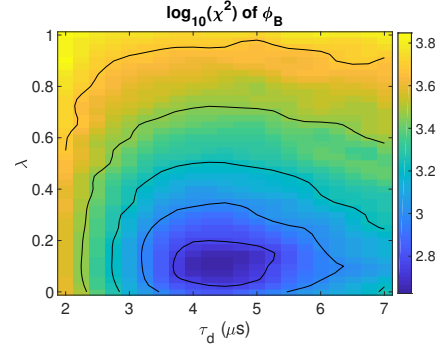


FIG. 6. Chi-square map for the conditional average of bursts,  $\phi_B$ , showing a minimum around  $(\tau_d, \lambda) = (4.5 \mu\text{s}, 0.10)$ . The black contours highlight the parabolic shape of the map. (Logarithmic scale used to improve visualization.) Position in TCABR:  $r = 19.5$  cm.

As indicated in Appendix A, due to pulse overlap, fitting the CAB with the analytical function can yield biased results. For this reason, we used chi-square maps to compare simulated and experimental CABs. The chi-square maps used here correspond to a grid least-squares method (similar to what is described in Sec. 8.1–8.3 of Ref. 47).

The chi-square can be defined as in Refs. 47 and 48,

$$\chi^2 = \sum_{j=1}^N \left( \frac{y_j - f_j(\vec{\theta})}{\sigma_j} \right)^2, \quad (26)$$

where  $y_j$  is the data,  $\sigma_j$  the uncertainty,  $f_j$  the function that fits  $y_j$ , and  $\vec{\theta}$  the vector of parameters. The uncertainty is composed by the experimental and simulated contributions,  $\sigma_j = (\sigma_{j,exp}^2 + \sigma_{j,sim}^2)^{0.5}$ . Supposing that both terms can be approximated by the standard deviation of repeated simulations (with fixed parameters), then the effective uncertainty is  $\sigma_j = \sqrt{2}\text{std}(f_j(\vec{\theta}))$ .

The objective of the  $\chi^2$  map is to obtain the parameter array  $\vec{\theta}$  that minimizes the chi-square. In the present case, the vector is  $\vec{\theta} = (\tau_d, \lambda)$  and  $y = \phi_B$  is the conditional average of bursts. In the analyzed experiment, the number of conditional events detected to compose  $\phi_B$  ranged from 400 to 560 bursts (Fig. 12). For the number of points to fit, we chose  $N = 81$ . As it will be later shown in Fig. 9(b),  $N = 81$  is sufficient to describe the rise and fall of the conditionally averaged bursts for all analyzed positions, as it corresponds to an interval of  $(N-1)\Delta t = 40 \mu\text{s}$  (i.e.,  $20 \mu\text{s}$  for each side), much higher than the pulse characteristic duration, which was always less than  $\tau_d = 6 \mu\text{s}$ .

As indicated in the second paragraph of this section, here  $f(\vec{\theta})$  is the CAB obtained from simulations, not from an analytical function. That is, for fixed parameters  $(\gamma, \langle A \rangle, I_0, \sigma_N)$  and a given pair  $(\tau_d, \lambda)$ , a synthetic saturation current signal was generated, and then its bursts were detected to make their

conditionally averaged waveform  $f$ . This simulated  $f$  was then compared to the experimental signal  $\phi_B$ . The procedure was repeated for a grid of parameters  $(\tau_d, \lambda)$ , aiming to find the pair that minimizes the  $\chi^2$  between simulated and experimental CABs. As further discussed in Appendix A, instead of using analytic expressions, fitting the experimental CABs with simulated ones avoids issues with pulse overlapping.

Fig. 6 shows the resultant chi-square map for the conditionally averaged burst of the TCABR position  $r = 19.5$  cm. With the help of the black contour lines, one sees that the map has a smooth parabolic format, ideal for finding a pair  $(\tau_d, \lambda)$  which minimizes the  $\chi^2$ .

### C. Fit of the PSD

Having fixed  $\gamma$ ,  $\langle A \rangle$ ,  $I_0$  and  $\sigma_N$  by the CF-fit (Subsec. IV A) and  $\tau_d$  and  $\lambda$  by the CAB fit (Subsec. IV B), it only remains to adjust the noise-balance parameter  $\lambda_N$  (defined in Eq. (20)). This can be achieved by fitting the power spectral density of  $I_{sat}$  with a Levenberg-Marquardt least-squares routine. Differently from the case of the characteristic function (Subsec. IV A), the points of the frequency spectrum are not correlated. The standard deviation of the PSD data is proportional to the average of the PSD,<sup>49</sup>

$$\sigma_\Omega(\omega) \propto \langle \Omega_I(\omega) \rangle \quad (27)$$

For this work, the frequency spectrum was set to have  $N = 2^{12} = 4096$  points. The PSDs were computed with MATLAB's *pwelch* function (which uses Welch's method)<sup>50</sup> and were multiplied by  $\pi\Delta t$  to match the theoretical spectra. Hanning windows with  $N = 2^{12}$  points were used, with an overlap of 50% with its neighbors.<sup>51</sup> Due to the averaging performed by Welch's method, the uncertainty of the spectrum was  $\sigma_\Omega(\omega) = 0.19\Omega_I(\omega)$ .

### D. Consistency of the fit

This subsection aims to show that the CF-CAB-PSD fit is consistent and to present a method for estimating uncertainties. For these purposes, 100 synthetic realizations of the pulse train model were created, all with  $N_{pt} = 8 \cdot 10^4$  points and true parameters

$$(\gamma, \langle A \rangle, I_0, \sigma_N) = (2, 7 \text{ mA}, 2 \text{ mA}, 1.5 \text{ mA}), \quad (28a)$$

$$(\tau_d, \lambda) = (5 \mu\text{s}, 0.1), \quad (28b)$$

$$\lambda_N = 0.6. \quad (28c)$$

These quantities are similar to the ones found in the scrape-off layer of TCABR (more specifically, at  $r = 19.5$  cm). For every synthetic realization, the fitting procedure was applied, and the fitted parameters were stored in the histograms of Fig. 7. With histograms like this, one can evaluate their standard deviations to estimate parameter uncertainties (this will be used in Fig. 10, 11, and 15). Simulations with different sets of possible parameters can also be produced to evaluate the uncertainty of a function (as done in Fig. 13). Finally, from

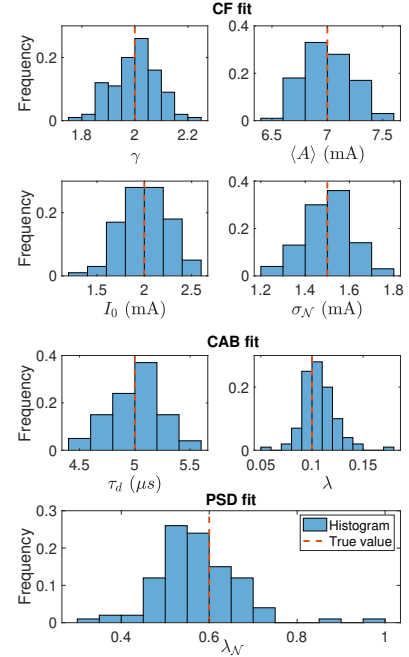


FIG. 7. Histograms of the CF-CAB-PSD fit, showing the results for 100 realizations of a synthetic  $I_{sat}$  signal with true values given by Eq. (28), which mimic the parameters of the position  $r = 19.5$  cm. The characteristic function (CF) fitted the first four parameters;  $\lambda$  and  $\tau_d$  were adjusted with the conditionally averaged burst (CAB);  $\lambda_N$  was evaluated with the power spectral density (PSD).

these histograms, one can calculate correlations between parameters. For the present case, the correlations are stored in Table IV of Appendix B.

All fitted parameters of Fig. 7 are well distributed around the true values, highlighted in orange in Fig. 7. This confirms that the model is consistent. Nonetheless, one may note that in Fig. 7 the fluctuation of the balance parameter  $\lambda_N$  is large,  $\sigma_{\lambda_N} = 0.09$ . This happened because, in the analyzed case, the noise level was too small,  $\epsilon = \sigma_N^2 / (\gamma \langle A \rangle^2) = 2.3\%$ , so that the contribution of the noise on the frequency spectrum is subtle. For a case with higher noise levels, as presented in Appendix B, the standard deviation of the fitted  $\lambda_N$  is smaller.

It should be noted that high frequencies of simulated power spectra are especially subject to the distortion known as aliasing (see for example pp. 95–98 of Ref. 52). To diminish this issue, we resampled the dynamical noise signals used in this manuscript. This was done by creating a noise signal  $I_D(t)$  with a doubled sample rate,  $2/\Delta t$ , which was then downsampled using an anti-aliasing low-pass filter of high order (in MATLAB, it can be done by using the *decimate* function). The noise variance also needed to be rescaled so that the re-

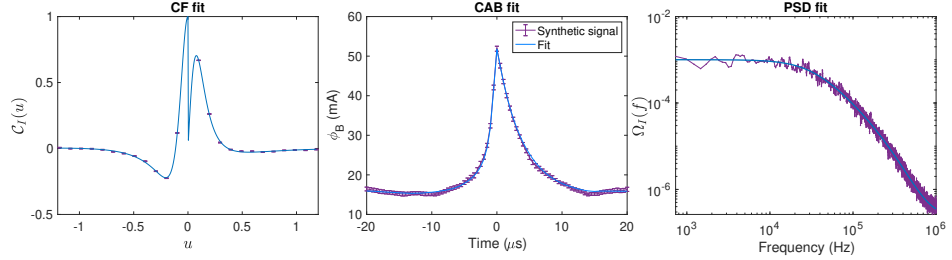


FIG. 8. Example of fit using the CF-CAB-PSD method, applied to a synthetic signal with parameters given by Eq. (28). For the CF and CAB, the uncertainties were estimated by repeated simulations with different sets of possible parameters (as explained in Subsec. IV D). For the PSD, they were estimated by  $\sigma_{\Omega_f}(f) = 0.19\Omega_f(f)$  (and were omitted to avoid polluting the figure).

sampled signal had the desired variance. If this resampling procedure was not applied in the synthetic signals, a systematic error would be introduced in the power spectrum and the estimation of  $\lambda_{\mathcal{N}}$  with this function would be biased. Finally, we underline that the signal distribution and conditionally averaged burst are not affected by the downsampling procedure.

Fig. 8 illustrates one example of fit with the CF-CAB-PSD method and a reference signal with true parameters given by Eq. (28). As expected, all three functions are well fitted.

## V. RESULTS IN TCABR

### A. Distributions, average bursts, and frequency spectra

In this subsection the fitting method presented in Sec. IV is applied to the TCABR tokamak, for three characteristic positions—at the plasma edge ( $r = 17.0$  cm), readily after the last closed flux surface ( $r = 18.5$  cm), and in the scrape-off layer ( $r = 19.5$  cm). With this, it is possible to analyze whether the pulse train model can describe the transition between the plasma edge,  $0.8 < r/a < 1$ , to the scrape-off layer (SOL),  $r/a > 1$  (where  $a = 18.0$  cm is TCABR's minor radius).

Each column of Fig. 9 corresponds to a position in TCABR, and each row depicts graphs with the same axes. The normalized saturation current was used,  $\tilde{I}_{sat} = (I_{sat} - \langle I_{sat} \rangle) / \sigma_I$  (Eq. (22)). The simulated graphs in blue were averaged with 30 Monte Carlo simulations, to diminish statistical fluctuations. Excerpts of  $\tilde{I}_{sat}$  can be seen in Fig. 4.

An increase of intermittency is observed for  $r = 18.5$  cm in the probability distribution functions (PDFs), Fig. 9(a). At the plasma-edge panel, the maximum value is about  $\tilde{I}_{sat} = 7$ , whereas after the last closed flux surface (LCFS),  $\tilde{I}_{sat} = 10$ . In the SOL, the maximum is  $\tilde{I}_{sat} = 8$ . Furthermore, it is noticeable that inside the plasma edge the PDF is closer to a Gaussian, indicating that the pulse overlap is high and the intermittency, low. Outside the confinement region, the PDF becomes more positively asymmetric, and its kurtosis and intermittency increase. The simulated distributions, obtained with the fitting

procedure of Sec. IV, are in excellent agreement with the experimental ones.

Fig. 9(b) shows the conditionally averaged burst shapes. On average the bursts are symmetric in the plasma edge, where the fitting method obtained  $\lambda = 0.548(32)$  for the pulse asymmetry parameter (Eq. (5)). As the radial position goes from the plasma edge to the SOL, the conditionally averaged waveforms become more asymmetric, with  $\lambda = 0.293(15)$  at  $r = 18.5$  cm and with  $\lambda = 0.105(13)$  at  $r = 19.5$  cm. The pulse characteristic duration also increases with  $r$ , going from  $\tau_d = 2.55(6)$   $\mu$ s to  $\tau_d = 3.81(7)$   $\mu$ s and  $\tau_d = 5.74(18)$   $\mu$ s, at  $r = 17.0$  cm,  $r = 18.5$  cm and  $r = 19.5$  cm, respectively.

With the exception of the data from  $r = 17.0$  cm, the conditionally averaged bursts shown in Fig. 9(b) aren't perfectly fitted by the model. As described in Chap. 5 of Ref. 17, bursts in TCABR are actually better described by stretched exponentials instead of the standard ones. Nevertheless, considering stretched pulse shapes would greatly increase the complexity of the model, as in this case the PDF of  $I_{sat}$  would also depend on the parameter  $\lambda$  and the CF would no longer be given by an analytic expression.

Finally, Fig. 9(c) shows the comparison between experimental power spectral densities and analytic PSDs from the model. In addition to the PSD from the mixed noise (MN) model, also included are the spectra from the model with observational (a.k.a. white) noise (ON) and with dynamical noise (DN). As expected, the curve from the mixed case is located in between the other two and, in the SOL, it is slightly closer to the experimental data. Nevertheless, for ON and DN, the PSD is not fitted, as the balance parameter is fixed ( $\lambda_{\mathcal{N}} = 0$  for ON and  $\lambda_{\mathcal{N}} = 1$  for DN). Conversely, as the only difference between the models with DN, ON, and MN is the noise-balance parameter  $\lambda_{\mathcal{N}}$ , all three have the same PDF and CAB, since these functions do not depend on  $\lambda_{\mathcal{N}}$  and this last was only used to fit the PSD.

In Fig. 9(c) it is seen that the model with the CF-CAB-PSD fitting method is unable to faithfully reproduce the tail of experimental PSDs in TCABR. It is possible to improve the spectra fit, adjusting  $\tau_d$ ,  $\lambda$ , and  $\lambda_{\mathcal{N}}$  with the PSD (that is, a CF-PSD fit instead of a CF-CAB-PSD fit). Neverthe-

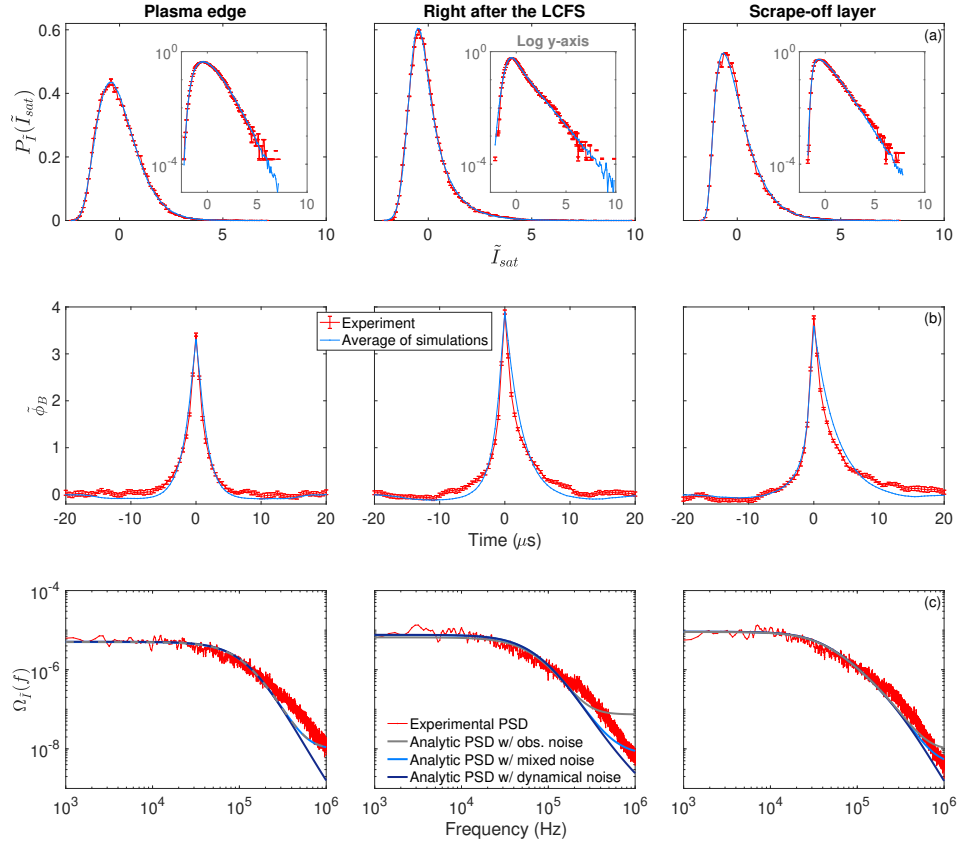


FIG. 9. In red, (a) PDFs, (b) conditionally averaged bursts, and (c) power spectra of  $\tilde{I}_{sat}$  for three positions—plasma edge ( $r = 17.0$  cm), right after the last closed flux surface ( $r = 18.5$  cm) and in the scrape-off layer ( $r = 19.5$  cm). The uncertainties were estimated with repeated simulations with fixed parameters. In light blue, average of simulations resultant from the CF-CAB-PSD fit (Sec. IV). Also shown are the analytical PSDs from observational, mixed, and dynamical noise, respectively in gray, light blue, and dark blue.

less, making this correction in the noise term would sacrifice information about bursts. The pulse duration and asymmetry parameters obtained by the CF-PSD fit would be smaller than the ones observed in the conditionally averaged bursts. Thus, the model isn't able to perfectly adjust the CAB and the PSD simultaneously in TCABR. Since extreme events, captured by the CAB, are important to the transport of particles and plasma-wall interactions,<sup>6,19</sup> the CF-CAB-PSD fit is more indicated than the CF-PSD one.

Moreover, in the CF-CAB-PSD method, a difference between the experimental and model PSD does not compromise the majority of the analysis, as only one parameter is fitted by the frequency spectrum and all the others are adjusted previously, being in good agreement with experimental data. Be-

sides, the analysis of the distribution parameters ( $\gamma$ ,  $\langle A \rangle$ ,  $I_0$ , and  $\sigma_N$ ), which will be presented in Subsec. VB, is independent of the choice between the CF-CAB-PSD and the CF-PSD fits, since the distribution parameters are evaluated with the CF, which is equally used in both methods.

Nonetheless, if one wants to prioritize the description of the plasma background over the bursts, it is possible to use the CF-PSD fit instead of the CF-CAB-PSD one.

## B. Radial profiles

Using the procedure described in Sec. IV, it is possible to fit the eight positions measured in the TCABR experiment. A

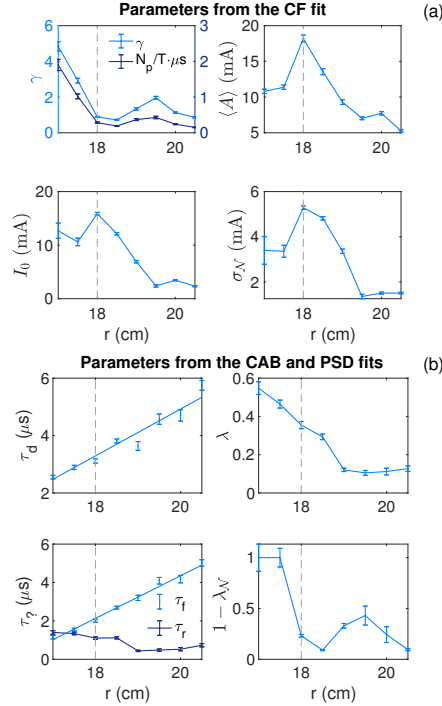


FIG. 10. (a) Radial profiles of the parameters fitted with the characteristic function for the eight radial positions measured in the TCABR experiment. Also included is the number of pulses per time, which was evaluated as  $N_p/T = \gamma/\tau_d$ . (b) Radial profiles of the parameters fitted with the CAB ( $\tau_d$ ,  $\lambda$ ) and PSD ( $\lambda_N$ ). Also included are the rise and fall pulse durations,  $\tau_r = \lambda \tau_d$  and  $\tau_f = (1 - \lambda) \tau_d$ . Uncertainties were estimated with repeated simulations with different sets of possible parameters (as explained in Subsec. IV D). The dashed line in  $r = a = 18.0$  cm indicates the beginning of the limiter.

radial profile of the obtained parameters is depicted in Fig. 10. (For the exact values, see Appendix B.)

The parameters of Fig. 10(a),  $\gamma$ ,  $\langle A \rangle$ ,  $I_0$ , and  $\sigma_N$ , define the probability distribution of the saturation current. Before  $r = a = 18.0$  cm, the intermittency parameter  $\gamma = \tau_d N_p/T$  achieves its biggest values, demonstrating that the pulse overlap is higher inside the plasma column than in the scrape-off layer. It quickly decays in the plasma edge, going from  $\gamma \approx 4.8$  at  $r = 17.0$  cm to  $\gamma \approx 0.8$  at  $r = a = 18.0$  cm. Moreover, the decrease of the other three parameters ( $\langle A \rangle$ ,  $I_0$ , and  $\sigma_N$ ) begins at  $r = a = 18.0$  cm and in general continues until the last measured position,  $r = 20.5$  cm. This decay is expected since the mean plasma density (proportional to  $\langle I_{sat} \rangle$ , Fig. 11(a)) also decreases with the radial profile.

For these four parameters of Fig. 10(a), a change of regime happens at  $r = a = 18.0$  cm, where  $a$  indicates the beginning

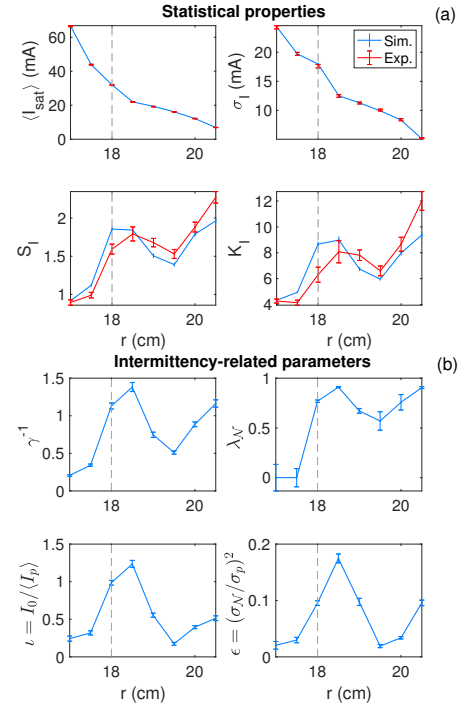


FIG. 11. (a) Four statistical properties of  $I_{sat}$ : mean, standard deviation, skewness, and kurtosis. Uncertainties were estimated with repeated simulations with fixed parameters. (b) The radial profiles of the parameters with a similar trend as the kurtosis. Uncertainties estimated with repeated simulations with different sets of possible parameters (as explained in Subsec. IV D). The dashed line marks the LCFS approximate position.

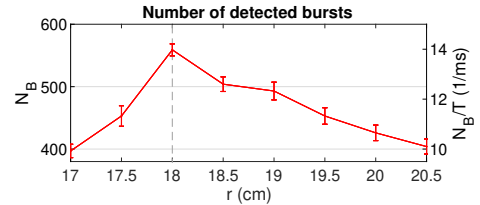


FIG. 12. Number of bursts in each position of the experiment. A pulse was detected as a burst if its peak was greater than  $\langle I_{sat} \rangle + 2.5\sigma_I$ . A minimum interval of  $15 \mu$ s was set between detections, to avoid counting the same event twice. Uncertainties were estimated with repeated simulations with fixed parameters.

of the limiter and thus the end of the plasma confinement region. The intermittency parameter  $\gamma = \tau_d N_p / T$  has a minimum at  $r = a$ , whereas the pulse average amplitude  $\langle A \rangle$ , the background  $I_0$ , and the noise standard deviation  $\sigma_N$  all have a maximum at this position. This is in accordance with the profile of the number of detected bursts ( $N_B$ , Fig. 12), which also has a maximum at  $r = a$  and a profile very similar to the one of the pulse average amplitude  $\langle A \rangle$ .

One possible explanation for the peaks in  $N_B$  and  $\langle A \rangle$  (Fig. 12 and 10(a)) is that the last closed flux surface at  $r = a$  has enhanced turbulence levels, which can give rise to high-amplitude bursts. From the perspective of the model, bursts are prevalent in high-intermittency regimes, marked by low  $\gamma$  (and thus large separation between pulses), as a high pulse overlap  $\gamma$  would hinder the distinction between bursts and background.<sup>22</sup> Finally, the high number of bursts around  $r = a = 18.0$  cm must be accompanied by an increase in the background  $I_0$  and in the noise standard deviation  $\sigma_N$ , so that the signal mean and variance do not decay more than they should due to the low  $\gamma$ . Also, bursts are more evident when the signal has a high background  $I_0$  and small fluctuations, in opposition to higher fluctuations that would arise due to greater values of  $\gamma$  and a lower background  $I_0$  (as happens at  $r = 17$  cm, position in which the pulse overlap  $\gamma$  is high (Fig. 10(a)) and the number of detected bursts, low (Fig. 12)). The high values of  $N_B$ ,  $\langle A \rangle$ ,  $I_0$ , and  $\sigma_N$  and the low value of  $\gamma$  at  $r = a$  could mean that the edge turbulence creates high-amplitude bursts at the same time that it shears mid-size pulses (related to  $\gamma$ ), transforming them into background plasma.

As for the graphs in Fig. 10(b), the behavior of  $\tau_d$  and  $\lambda$  was already anticipated in the discussion of Fig. 9(b), Subsec. V A. One sees that the pulse characteristic duration  $\tau_d$  increases linearly with the radial position, going from  $\tau_d \approx 2.5$   $\mu$ s at  $r = 17.0$  cm to  $\tau_d \approx 5.7$   $\mu$ s at  $r = 20.5$  cm. The pulse asymmetry parameter  $\lambda$ , on the other hand, is compatible with  $\lambda = 0.5$  in the plasma edge (indicating symmetric pulses on average) and then decays to  $\lambda = 0.1$  in the far scrape-off layer (indicating asymmetric pulses). This duration and asymmetry of bursts in the SOL have similarities with the shape of comets, which have a large tail (that is,  $\lambda < 0.5$ , in the nomenclature of the model). Just as the radiation pressure of stars shapes the tails of comets, the resistance of the background plasma to the transport of bursts may account for their quick rise and slow fall in the SOL.

In its turn, the linear enlargement of the burst tail could be a consequence of the natural spread that these structures suffer while their amplitude decreases when crossing the scrape-off layer. Supporting the shape similarity between bursts with comets, in the panel of  $\tau_f$  and  $\tau_r$  of Fig. 10(b) it is seen that the fall duration  $\tau_f = (1 - \lambda)\tau_d$  linearly increases with the position, just as  $\tau_d$ . The pulse rise duration, on the contrary, is approximately constant in  $r \in [17, 18.5]$  cm, then decays a little in  $r = 19.0$  cm and is constant thereafter again.

In Fig. 10(b), it remains to analyze the noise-balance parameter, defined as the ratio between the variances of dynamical and total noise,  $\lambda_N = \sigma_D^2 / \sigma_N^2$ . It is easier to interpret the profile of this parameter if it is portrayed from the perspective of observational noise,  $1 - \lambda_N = \sigma_D^2 / \sigma_N^2$ , as depicted in Fig.

10(b). The profile of the observational noise ratio  $\sigma_D^2 / \sigma_N^2$  is similar to the one of the overlap parameter  $\gamma = \tau_d N_p / T$  (Fig. 10(a)). Both have high values on the plasma edge, present a local minimum around  $r = 18.5$  cm, and a local maximum around  $r = 19.5$  cm. For this reason, we infer that the proportion of observational noise accompanies the pulse overlap: more pulses implies higher plasma activity, which may enhance measurement noise. Furthermore, inside the plasma column, the levels of diffusion transport are higher than in the SOL.<sup>6,53</sup> Since diffusion measured at a fixed point is modeled by white noise, it makes sense that the uncorrelated-noise levels are higher in the plasma edge. Conversely, as diffusion is lower in the SOL,<sup>6,53</sup> dynamical noise prevails in this region ( $\sigma_D^2 / \sigma_N^2 > 0.5$ ).

Regarding the statistical properties (Fig. 11(a)), one sees that the average and standard deviation of  $I_{sat}$  monotonically decay with the position. This is expected since the density also decreases from the plasma column to the SOL. In contrast, the skewness and kurtosis of  $I_{sat}$  ( $S_I = \langle \bar{I}_{sat}^3 \rangle$  and  $K_I = \langle \bar{I}_{sat}^4 \rangle$ ) tend to increase with  $r$ . Inside the plasma column, their values are relatively small, close to the ones of a Gaussian distribution, which has  $S_I = 0$  and  $K_I = 3$ . This is in accordance with the high pulse overlap  $\gamma$  that was obtained by the model for  $r < 18.0$  cm (Fig. 10(a)) and which leads to Gaussian-like distributions.<sup>22</sup> At the minor radius,  $r = a = 18.0$  cm, the skewness and kurtosis of  $I_{sat}$  greatly increased, by about 50%. Thereafter, they passed through a local maximum at  $r = 18.5$  cm and a local minimum at  $r = 19.5$  cm. This behavior may be accounted for by a conjunction of two effects. Firstly, the last closed flux surface is subject to high turbulence levels, which can generate extreme events (as seen in the peak of Fig. 12). Thus, at the near SOL, it is expected that the skewness and kurtosis have high values. As the position departs from the LCFS, this effect is gradually reduced, and a minimum in  $S_I$  and  $K_I$  is achieved at  $r = 19.5$  cm. Nevertheless, the transport in the SOL is mainly due to convection<sup>6,53</sup> and thus mid-size pulses outlive in the far SOL, which could explain the increase in the skewness and kurtosis again after  $r = 19.5$  cm.

We highlight that, as skewness and kurtosis are strongly affected by rare events, different experiments with the same initial conditions may present moderately different profiles of  $S_I$  and  $K_I$  due to statistical fluctuations. For example, the local maximum and minimum at  $r = 18.5$  cm and  $r = 19.5$  cm could be replaced by a plateau in this region, or the profiles could monotonically increase, with a small deceleration between  $r = 18.5$  cm and  $r = 19.5$  cm.

The skewness and kurtosis are directly related to some parameters of the stochastic model. One sees in Fig. 11 that  $S_I$ ,  $K_I$ ,  $\gamma^{-1}$ ,  $t \equiv I_0 / \langle I_p \rangle$ ,  $\varepsilon \equiv \sigma_N^2 / \sigma_p^2$  and  $\lambda_N \equiv \sigma_D^2 / \sigma_N^2$  have a similar profile, with a local maximum and minimum respectively at  $r = 18.5$  cm and  $r = 19.5$  cm. There is a well-known parabolic relation between skewness and excess kurtosis for density fluctuations in magnetized plasmas:  $K_I - 3 \approx 1.5 S_I^2$ .<sup>5,8,11,21,22,26,30,31</sup> Also, from Eq. (9), it is possible to write the connection between  $K_I$ ,  $\gamma^{-1} = \tau_w / \tau_d$  and

Physics of Plasmas

$\varepsilon = \sigma_{\mathcal{N}}^2 / \sigma_p^2$ , as

$$K_I - 3 = \frac{6\gamma^{-1}}{(1 + \varepsilon)^2}. \quad (29)$$

For small noise fluctuations  $\varepsilon$ , the excess kurtosis is approximately equal to the intermittency level  $\gamma^{-1}$  times a constant,  $K_I - 3 \approx 6\gamma^{-1}$ . Furthermore, since  $\langle I_p \rangle = \gamma \langle A \rangle$  and  $\sigma_p^2 = \gamma \langle A \rangle^2$ , then the relative mean and variance of the background can be respectively written as  $\iota = \gamma^{-1} I_0 / \langle A \rangle$  and  $\varepsilon = \gamma^{-1} \sigma_{\mathcal{N}}^2 / \langle A \rangle^2$ . Thus both are also proportional to the intermittency level  $\gamma^{-1}$  and it makes sense that the three vary together. Finally, the relation between  $\gamma^{-1}$  and  $\lambda_{\mathcal{N}}$  was already explained in the discussion of Fig. 10, but using their duals,  $\gamma$  and  $1 - \lambda_{\mathcal{N}}$ . To conclude, even if the skewness and kurtosis profiles were moderately different in other experiments (as described in the previous paragraph), the relation between them and the parameters  $\gamma^{-1}$ ,  $\iota$ ,  $\varepsilon$  and  $\lambda_{\mathcal{N}}$  would remain, as they are all linked by  $\gamma^{-1}$ .

### C. Comparing different types of noise

To compare dynamical, observational, and mixed noise, we propose the use of the determinism (DET) from recurrence quantification analysis.<sup>33,34,36</sup> RQA diagnostics unveil dynamical properties of the signal that are not evident from the data series.<sup>33,36</sup> More specifically, DET quantifies the percentage of diagonal lines that are recurrent in the recurrence plot.<sup>33,34,37</sup> This means the RQA determinism is high when the signal evolution is similar in different time intervals, which is expected to occur when the signal dynamics are dominated by deterministic rules. For example, chaotic time series tend to have a higher determinism than stochastic ones. The minimum value of DET happens for white noise (DET = 0.188 for the used RQA parameters), in which case all recurrences occur by chance and are isolated in the recurrence plots. Conversely, the maximum value of DET is 1, which only occurs for numerical fully deterministic signals with maximal Lyapunov exponent close to zero. For example, periodic signals have DET = 1.

To obtain DET of  $I_{sat}$ , we used an embedding dimension of  $d_{RQA} = 4$ , as well as a delay of  $\tau_{RQA} = 10$  points (5  $\mu$ s) and repeated windows of  $N_{RQA} = 10^3$  points to evaluate the average and standard deviation of DET. The recurrence rate was fixated at RR = 10%. The values for these four parameters were based on previous works in magnetized plasmas<sup>33–35</sup> and moderate changes in them do not alter the results.

The red curve in Fig. 13 represents the profile of the experimental RQA determinism. It slightly increases with  $r$  and the most noticeable change occurred in the transition from the plasma edge to the SOL ( $r = 17.5$  cm to  $r = 18.0$  cm). In gray, data obtained with white noise ( $\lambda_{\mathcal{N}} = 0$ ) are shown. There is an obvious structure with a minimum at  $r = 18.5$  cm and maximum at  $r = 19.5$  cm. We infer that, for the signal with white/observational noise, the RQA determinism is inversely proportional to the noise level  $\varepsilon = \sigma_{\mathcal{N}}^2 / \sigma_p^2$ , whose profile also has local extrema at  $r = 18.5$  cm and  $r = 19.5$  cm (Fig. 11(b)).

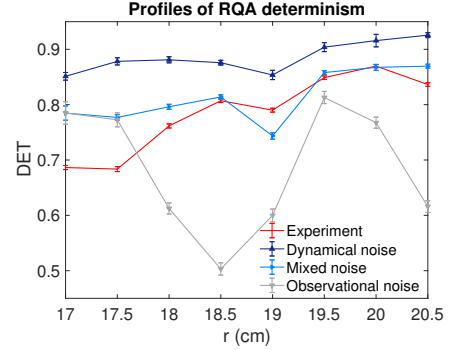


FIG. 13. Radial profiles of the determinism obtained with recurrence quantification analysis (RQA). In red, the data from the TCABR experiment; in dark blue, light blue, and gray are the data from SPTM simulations with DN, MN, and ON, respectively. All have the same parameters as in Fig. 10, except for the noise balance  $\lambda_{\mathcal{N}}$  ( $\lambda_{\mathcal{N}} = 1$  for DN,  $0 \leq \lambda_{\mathcal{N}} \leq 1$  for MN, and  $\lambda_{\mathcal{N}} = 0$  for ON). The uncertainties in the synthetic signals were estimated with repeated simulations with different sets of possible parameters (as explained in Subsec. IV D), while the ones in the experimental data were obtained by evaluating DET in windows of  $N_{RQA} = 10^3$  points of  $I_{sat}$  and then taking the standard deviation of the mean. The dynamical noise in the simulations was resampled (penultimate paragraph of Subsec. IV D), obtaining slightly higher values of DET when compared to signals without resampling. Still, this increase was within the error bars.

On the other hand, the dark blue curve in Fig. 13 shows the DET obtained with dynamical noise ( $\lambda_{\mathcal{N}} = 1$ ). The simulations with DN have higher RQA determinism than the ones with observational noise. This is logical, since white noise can create isolated recurrences, decreasing DET, while dynamical noise increases correlations in the signal, which can produce not-isolated recurrences that increase DET. Nevertheless, the RQA determinism of the data with dynamical noise was systematically higher than the experimental ones.

Lastly, the light blue curve in Fig. 13 depicts the RQA determinism obtained with a mixture of observational and dynamical noise, with the balance parameter  $\lambda_{\mathcal{N}}$  fitted by the PSD. As expected, this simulated data is situated in between the two other noise models, as in this case balance parameter is  $0 \leq \lambda_{\mathcal{N}} \leq 1$ . Moreover, the profile of DET of the mixed noise case was the closest to the experimental one. This makes sense since in general it is expected that the signal is simultaneously composed of measurement and dynamical noise.

We note that at the plasma edge ( $r < 18.0$  cm), the experimental DET was lower than all the simulated cases. This indicates that at this region the experimental signal has a dynamical aspect that the model and fit weren't able to capture.

## VI. CONCLUSION

The presented analysis aims to contribute to the ongoing characterization of SOL fluctuations using a stochastic description. We developed a procedure to fit all the parameters of the stochastic pulse train model<sup>21–25</sup> considering double-exponential pulses and a mixture of dynamical and measurement noise. This method can be used in tokamaks to objectively fit the model parameters in order to describe density fluctuations. In special, by comparing simulated and experimental conditionally averaged bursts, the procedure provides unbiased values for the pulse asymmetry and duration. In other words, this method prevents distortions due to pulse overlapping that would occur in a simple analytic fit of the conditionally averaged burst.

The model and the proposed fit were then applied to the TCABR tokamak. Although bursts have already been described in limited tokamaks,<sup>6,18,54</sup> this is the first article to employ the stochastic pulse train model to a limited plasma. Thus, the present work helps to demonstrate the universality of the model description and its validation for one more type of machine. Previously, the stochastic model was used in diverted<sup>8–13,26–31</sup> and spherical<sup>55</sup> tokamaks and to a Helimak.<sup>14,32</sup> For future works, it would be interesting to apply the model to stellarators and other types of devices with magnetically confined plasmas.

The relatively low temperature in TCABR allowed the analysis of radial positions within the plasma edge and over a wide range of the scrape-off layer. As observed in other tokamaks,<sup>9,11,13,29,30</sup> in TCABR the saturation current distribution was well described by a superposition of Gamma-distributed pulses and additive Gaussian noise. Inside the plasma column, the PDF was closer to a Gaussian, while in the scrape-off layer it was more positively skewed.

Moreover, in this article, radial profiles of all SPTM parameters were attentively analyzed, in order to unveil the correspondence between the model parameters and experimental density fluctuations. At the last closed flux surface, which separates the plasma edge and SOL, the number of detected bursts was the highest. The parameters of pulse separation and average amplitude also had a peak in the LCFS, indicating a regime of strong intermittency there. Furthermore, we showed evidence that the pulse separation, the plasma background, and noise levels (normalized by the correspondent pulse contributions) follow the same trend as the skewness and kurtosis of density fluctuations.

The radial analysis further illustrated that the pulse overlap is high inside the plasma column of TCABR, in agreement with the expectation that plasma pulses are created inside the plasma column and move outward. Since just a portion of the particles travels to the SOL, this also explains why the pulse overlap, average amplitude, background plasma, and noise fluctuations were smaller in the far scrape-off layer than in the plasma edge. Finally, it was observed that the pulse fall duration linearly increased with the position, which may be a consequence of the natural spread and decrease of amplitude that the pulses suffer when traveling across the scrape-off layer. This linear increase can be investigated in other toka-

maks and, if it shows to be universal, it can be used in future works to model the evolution of bursts and blobs in magnetized plasmas.

Lastly, we introduced the determinism from recurrence quantification analysis<sup>33–37</sup> to distinguish what type of noise reproduces better the background of experimental signals. At the plasma edge, uncorrelated noise prevailed, which makes sense since high plasma activity can lead to higher measurement noise. Also, the rate of diffusion (related to uncorrelated noise) is greater in the edge than in the SOL.<sup>6</sup> In contrast, in the SOL the noise related to the dynamics of the signal predominated, probably because of the high convection levels there. Convection is associated with the transport of coherent structures, which are time-correlated, just as dynamical noise. Nevertheless, some portion of measurement noise was still present in the SOL, indicating that a mixture of observational and dynamical noise can occur in density fluctuations of magnetized plasmas.

To summarize, in this paper we introduced a fitting method for the stochastic pulse train model with mixed noise. This fitting routine can be applied to different tokamaks in the context of the SPTM, to characterize plasma fluctuations. The fit and model were then applied for the TCABR tokamak for the first time and several features of plasma fluctuations were described. In special, the distribution of ion saturation current was in excellent agreement with the model. Thereafter, radial profiles of the SPTM parameters were presented, revealing a clear distinction between the plasma edge and SOL and also a direct relationship between the saturation current kurtosis, the intermittency of the pulses, and background parameters. A linear increase with the radial position was also found in the pulse fall duration. Finally, using the determinism from recurrence quantification analysis, we showed evidence that observational noise prevails in the plasma edge of TCABR, whereas in the SOL a mixture of both observational and dynamical noise may exist, with a predominance of dynamical noise.

## ACKNOWLEDGMENTS

This work was financially supported by the Brazilian agencies São Paulo Research Foundation (FAPESP), grants 2018/03211-6 and 2020/03912-4, and CNPq, grants 312771/2019-3 and 131254/2020-0. We acknowledge G. G. Grenfell and the TCABR team for providing the experimental data which was analyzed in this article. We are also grateful to the editor and referees for their constructive comments.

## DATA AVAILABILITY

The data that support the findings of this study are available from the corresponding author upon reasonable request.

## Appendix A: Analytic fit of the CAB

In this work, instead of analytically fitting the experimental conditionally averaged burst, we determined the pulse shape parameters ( $\tau_d$  and  $\lambda$ ) by comparing the experimental CAB with simulated ones. This was employed to reduce the influence of the pulse overlapping and discrete-time resolution comparable with the burst characteristic rise time, as explained in this Appendix. We started by considering that it is reasonable to fit conditionally averaged bursts with an analytic function,

$$\phi_B(t) = c_1 + c_2 \phi(t/\tau_d; \lambda) \quad (\text{A1})$$

where the pulse shape  $\phi$  is given by a double exponential (Eq. (5)) and  $c_1$  and  $c_2$  are constants to be fitted together with  $\tau_d$  and  $\lambda$ . The top panel of Fig. 14 shows, in yellow, the analytic fit of the experimental CAB of the position  $r = 17.0$  cm. The adjustment is in great accordance with the experimental data. However, making a simulation with the parameters obtained by this analytic fit yields an averaged burst (in dark blue) that is larger than the experimental one (in red). This happens due to overlapping, which creates bursts larger than the individual pulses. In general, such effect is important where the pulse overlap  $\gamma$  is large (in TCABR,  $r < a = 18$  cm).

To mitigate this problem, it is possible to fit the burst parameters by comparing simulated and experimental CABs. With this method, the duration and asymmetry of the simulated CAB are not compared directly to the ones of the experimental CAB. Instead, a grid of parameters ( $\tau_d, \lambda$ ) is used to create simulations corresponding to each pair. Then, the pair that gives the minimum  $\chi^2$  value between simulated and experimental CABs is chosen. In other words, the overlapping effect is mitigated since, in this procedure, it is the true parameters from the individual pulses that are used to minimize the  $\chi^2$ . Also, simulated CABs pass through the same overlapping process that the experimental ones do. This is exemplified in the bottom panel of Fig. 14, which depicts a unitary pulse with duration and asymmetry parameters fitted with simulations. (Also, for comparison, its amplitude was chosen equal to the one of the conditionally averaged burst.) Due to pulse-overlapping, the averaged structure (in light blue) is larger and less asymmetric than the unitary pulse, being closer to the experimental CAB than the one (in dark blue) obtained with parameters calculated by the analytic fit.

Fig. 15 compares the radial profiles of the parameters  $\tau_d$  and  $\lambda$  obtained by the analytic fit (dark blue) and the adjustment with simulations (light blue). For the plasma edge, which has high pulse overlap, the characteristic durations obtained by the analytic fit are larger than the ones found by the adjustment with simulations. In addition to the high-overlap effect, if the rise duration  $\tau_r = \lambda \tau_d$  is close to the temporal resolution of measurements,  $\Delta t = 0.5 \mu\text{s}$ , then the pulse shape in the CAB may also be distorted. As seen in the bottom panel of Fig. 15, these overlapping and resolution effects also make the bursts detected at the SOL to be on average less asymmetric than the original pulses.

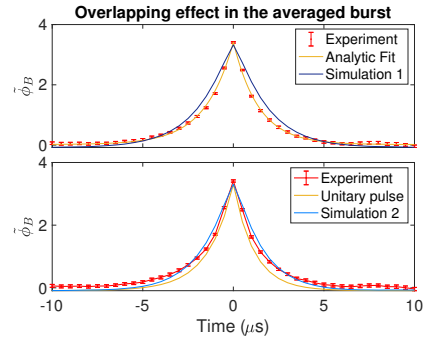


FIG. 14. Top panel: experimental CAB of position  $r = 17.0$  cm (in red), its analytic fit (in yellow), and the corresponding averaged simulation (in dark blue) using the parameters  $\tau_d$  and  $\lambda$  obtained by the analytic fit. Bottom panel: the same experimental CAB (in red), together with the simulated one (in light blue) obtained by fitting the averaged burst with simulations (as done in Subsec. IV B). Also shown is a unitary simulated pulse (yellow), shorter and more asymmetric than the corresponding conditional average in blue. Both simulations corresponding to the dark and light blue curves have the same parameters, with exception to  $\tau_d$  and  $\lambda$ . The error bars were estimated with repeated simulations with fixed parameters.

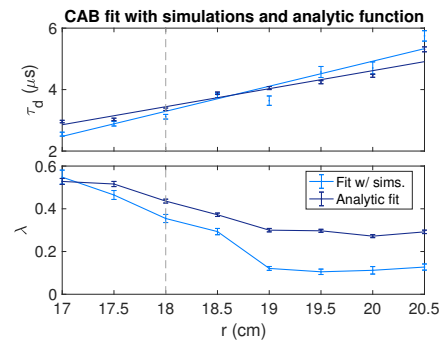


FIG. 15. Radial profiles of the parameters fitted with the conditionally averaged burst (CAB). In light blue are the results from the fit with simulations (as in Subsec. IV B). In dark blue are the results from a fit with the analytic function (Eq. (A1)). The uncertainties in the analytic fit were estimated by the own procedure, while the ones in the numeric fit were obtained with repeated simulations with different sets of possible parameters (as explained in Subsec. IV D). The dashed line indicates the minor radius  $a = 18.0$  cm.

TABLE II. Parameters fitted with the characteristic function. Uncertainties estimated with repeated simulations with different set of possible parameters (as explained in Subsec. IV D).

| $r$ (cm) | $\gamma$ | $\langle A \rangle$ (mA) | $I_0$ (mA) | $\sigma_{\mathcal{N}}$ (mA) |
|----------|----------|--------------------------|------------|-----------------------------|
| 17.0     | 4.84(26) | 10.80(31)                | 12.7(14)   | 3.4(6)                      |
| 17.5     | 2.92(13) | 11.38(29)                | 10.6(7)    | 3.36(27)                    |
| 18.0     | 0.89(3)  | 18.20(48)                | 15.88(24)  | 5.29(8)                     |
| 18.5     | 0.72(3)  | 13.56(42)                | 12.13(22)  | 4.82(8)                     |
| 19.0     | 1.34(6)  | 9.30(33)                 | 6.90(22)   | 3.36(10)                    |
| 19.5     | 1.96(8)  | 7.02(19)                 | 2.39(22)   | 1.36(10)                    |
| 20.0     | 1.13(4)  | 7.73(23)                 | 3.45(12)   | 1.51(4)                     |
| 20.5     | 0.86(4)  | 5.26(16)                 | 2.32(10)   | 1.51(3)                     |

TABLE III. Parameters obtained with the conditionally averaged burst ( $\tau_d$  and  $\lambda$ ) and with the PSD ( $\lambda_{\mathcal{N}}$ ). Uncertainties estimated with repeated simulations with different set of possible parameters (as explained in Subsec. IV D).

| $r$ (cm) | $\tau_d$ ( $\mu$ s) | $\lambda$ | $\lambda_{\mathcal{N}}$ |
|----------|---------------------|-----------|-------------------------|
| 17.0     | 2.55(6)             | 0.548(32) | 0.00(13)                |
| 17.5     | 2.89(8)             | 0.465(21) | 0.00(9)                 |
| 18.0     | 3.12(8)             | 0.355(19) | 0.768(12)               |
| 18.5     | 3.81(7)             | 0.293(15) | 0.910(5)                |
| 19.0     | 3.64(15)            | 0.121(9)  | 0.671(23)               |
| 19.5     | 4.57(18)            | 0.105(13) | 0.57(9)                 |
| 20.0     | 4.70(20)            | 0.112(18) | 0.76(8)                 |
| 20.5     | 5.75(17)            | 0.127(14) | 0.905(10)               |

TABLE IV. Correlations of the parameters obtained in Subsec. IV D. In bold, the correlations with absolute value above 50%, which correspond to the CF-fit parameters.

|                         | $\gamma$     | $\langle A \rangle$ | $I_0$        | $\sigma_{\mathcal{N}}$ | $\tau_d$ | $\lambda$ | $\lambda_{\mathcal{N}}$ |
|-------------------------|--------------|---------------------|--------------|------------------------|----------|-----------|-------------------------|
| $\gamma$                | 1            | <b>-0.92</b>        | <b>-0.91</b> | <b>-0.70</b>           | -0.30    | -0.36     | -0.16                   |
| $\langle A \rangle$     | <b>-0.92</b> | 1                   | <b>0.71</b>  | <b>0.56</b>            | 0.35     | 0.33      | 0.05                    |
| $I_0$                   | <b>-0.91</b> | <b>0.71</b>         | 1            | <b>0.78</b>            | 0.16     | 0.34      | 0.27                    |
| $\sigma_{\mathcal{N}}$  | <b>-0.70</b> | <b>0.56</b>         | <b>0.78</b>  | 1                      | 0.12     | 0.32      | 0.46                    |
| $\tau_d$                | -0.30        | 0.35                | 0.16         | 0.12                   | 1        | -0.06     | -0.39                   |
| $\lambda$               | -0.36        | 0.33                | 0.34         | 0.32                   | -0.06    | 1         | -0.46                   |
| $\lambda_{\mathcal{N}}$ | -0.16        | 0.05                | 0.27         | 0.46                   | -0.39    | -0.46     | 1                       |

#### Appendix B: Obtained parameters and correlations

Tables II and III show the parameters obtained with the CF-CAB-PSD fit of Sec. IV, for the eight positions measured in TCABR. The simulations of Sec. V were made from these values.

Table IV presents the correlations of the parameters evaluated in Subsec. IV D. The correlations were estimated using synthetic realizations of the pulse train model, with parameters similar to the ones found in the position  $r = 19.5$  cm of TCABR. Simulating other positions yields similar correlations.

Finally, Fig. 16 shows the parameter histograms obtained by applying the same procedure of Subsec. IV D, but for a

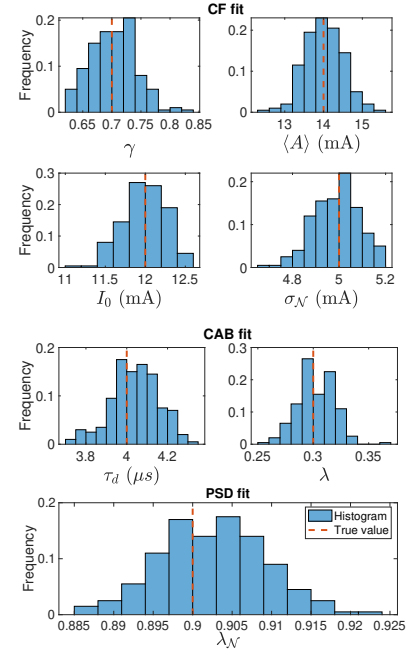


FIG. 16. Histograms of the CF-CAB-PSD fit, showing the results for 200 realizations of a synthetic  $I_{sar}$  signal with true values given by Eq. (B1), which mimic the parameters of the position  $r = 18.5$  cm. The characteristic function (CF) fitted the first four parameters;  $\lambda$  and  $\tau_d$  were adjusted with the conditionally averaged burst (CAB);  $\lambda_{\mathcal{N}}$  was evaluated with the power spectral density (PSD).

simulation that mimics position  $r = 18.5$  cm in TCABR,

$$(\gamma, \langle A \rangle, I_0, \sigma_{\mathcal{N}}) = (0.7, 14 \text{ mA}, 12 \text{ mA}, 5 \text{ mA}), \quad (\text{B1a})$$

$$(\tau_d, \lambda) = (4 \mu\text{s}, 0.3), \quad (\text{B1b})$$

$$\lambda_{\mathcal{N}} = 0.9. \quad (\text{B1c})$$

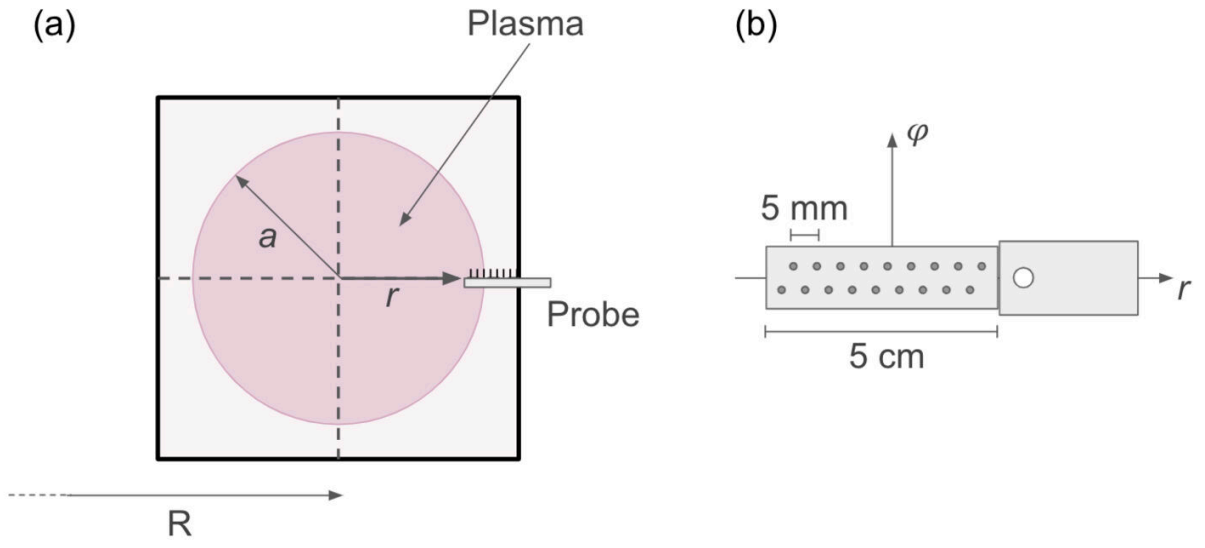
Compared to the position  $r = 19.5$  cm, which was described in Subsec. IV D, the position  $r = 18.5$  cm has lower pulse overlap  $\gamma$  and higher pulse average amplitude  $\langle A \rangle$ , noise level  $\varepsilon = \sigma_{\mathcal{N}}^2 / (\gamma \langle A \rangle^2) = 25\%$ , and noise-balance parameter  $\lambda_{\mathcal{N}}$ . The histogram of the noise balance has a much lower standard deviation,  $\sigma_{\lambda_{\mathcal{N}}} = 0.007$ , when compared to the one obtained for the  $r = 19.5$  cm position,  $\sigma_{\lambda_{\mathcal{N}}} = 0.09$ . This happened because the first had a greater noise level  $\varepsilon = 25\%$ , when compared to the second,  $\varepsilon = 2.3\%$ . Thus, for  $r = 18.5$  cm, the power spectrum is more sensitive for changes in  $\lambda_{\mathcal{N}}$  and the parameter fit is more precise.

## REFERENCES

- <sup>1</sup>S. I. Krasheninnikov, D. A. D'Ippolito, and J. R. Myra, *Journal of Plasma Phys.* **74**, 679–717 (2008).
- <sup>2</sup>A. Fasoli, I. Furno, and P. Ricci, *Nat. Phys.* **15**, 872 (2019).
- <sup>3</sup>B. LaBombard, R. L. Boivin, M. Greenwald, J. Hughes, B. Lipschultz, D. Mossessian, C. S. Pitcher, J. L. Terry, S. J. Zweben, and Alcator Group, *Phys. Plasmas* **8**, 2107 (2001).
- <sup>4</sup>A. Y. Pigarov, S. I. Krasheninnikov, T. D. Rognlien, M. J. Schaffer, and W. P. West, *Phys. Plasmas* **9**, 1287 (2002).
- <sup>5</sup>D. A. D'Ippolito, J. R. Myra, and S. J. Zweben, *Phys. Plasmas* **18**, 060501 (2011).
- <sup>6</sup>G. Y. Antar, G. Counsell, Y. Yu, B. Labombard, and P. Devynck, *Phys. Plasmas* **10**, 419 (2003).
- <sup>7</sup>S. J. Zweben, G. Y. Antar, G. Counsell, Y. Yu, B. Labombard, and P. Devynck, *Plasma Phys. Controlled Fusion* **58**, 044007 (2016).
- <sup>8</sup>O. E. Garcia, R. Kube, A. Theodorsen, B. LaBombard, and J. L. Terry, *Phys. Plasmas* **25**, 056103 (2018).
- <sup>9</sup>A. Theodorsen, O. E. Garcia, R. Kube, B. LaBombard, and J. L. Terry, *Phys. Plasmas* **25**, 122309 (2018).
- <sup>10</sup>O. E. Garcia, J. Horacek, and R. A. Pitts, *Nucl. Fusion* **55**, 062002 (2015).
- <sup>11</sup>O. E. Garcia, R. Kube, A. Theodorsen, J.-G. Bak, S.-H. Hong, H.-S. Kim, the KSTAR Project Team, and R. A. Pitts, *Nucl. Mater. Energy* **12**, 36–43 (2017).
- <sup>12</sup>N. R. Walkden, A. Wynn, F. Militello, B. Lipschultz, G. Matthews, C. Guillemaut, J. Harrison, and D. Moulton, *Nucl. Fusion* **57**, 036016 (2017).
- <sup>13</sup>A. Bencze, M. Berta, A. Buzás, P. Hacek, J. Krbec, M. Szutyányi, and the COMPASS Team, *Plasma Phys. Controlled Fusion* **61**, 085014 (2019).
- <sup>14</sup>F. A. C. Pereira, I. M. Sokolov, D. L. Toufen, Z. O. Guimarães-Filho, I. L. Caldas, and K. W. Gentle, *Phys. Plasmas* **26**, 052301 (2019).
- <sup>15</sup>F. A. C. Pereira, W. A. Hernandez, D. L. Toufen, Z. O. Guimarães-Filho, I. L. Caldas, and K. W. Gentle, *Phys. Plasmas* **25**, 042301 (2018).
- <sup>16</sup>W. A. Hernandez, Z. O. Guimarães-Filho, G. G. Grenfell, and I. C. Nascimento, *J. Plasma Phys.* **85**, 905850407 (2019).
- <sup>17</sup>W. A. H. Baquero, *Turbulent temperature fluctuations in TCABR tokamak*, Ph.D. thesis, University of Sao Paulo (2017).
- <sup>18</sup>A. A. Ferreira, M. V. A. P. Heller, I. L. Caldas, E. A. Lerche, L. F. Ruchko, and L. A. Baccalá, *Plasma Phys. Controlled Fusion* **46**, 669 (2004).
- <sup>19</sup>R. A. Pitts, J. P. Coad, D. P. Coster, G. Federici, W. Fundamenski, J. Horacek, K. Krieger, A. Kukushkin, J. Likonen, G. F. Matthews, M. Rubel, J. D. Strachan, and JET-EFDA contributors, *Plasma Phys. Controlled Fusion* **47**, B303 (2005).
- <sup>20</sup>D. G. Whyte, B. L. Lipschultz, P. C. Stangeby, J. Boedo, D. L. Rudakov, J. G. Watkins, and W. P. West, *Plasma Phys. Controlled Fusion* **47**, 1579 (2005).
- <sup>21</sup>O. E. Garcia, *Phys. Rev. Lett.* **108**, 265001 (2012).
- <sup>22</sup>O. E. Garcia, R. Kube, A. Theodorsen, and H. L. Pécseli, *Phys. Plasmas* **23**, 052308 (2016).
- <sup>23</sup>O. E. Garcia and A. Theodorsen, *Phys. Plasmas* **24**, 032309 (2017).
- <sup>24</sup>A. Theodorsen, O. E. Garcia, and M. Rypdal, *Phys. Scr.* **92**, 054002 (2017).
- <sup>25</sup>A. Theodorsen and O. E. Garcia, *Plasma Phys. Controlled Fusion* **60**, 034006 (2018).
- <sup>26</sup>O. E. Garcia, S. M. Fritzner, R. Kube, I. Cziegler, B. LaBombard, and J. L. Terry, *Phys. Plasmas* **20**, 055901 (2013).
- <sup>27</sup>A. Theodorsen, O. E. Garcia, R. Kube, B. LaBombard, and J. L. Terry, *Nucl. Fusion* **57**, 114004 (2017).
- <sup>28</sup>R. Kube, A. Theodorsen, O. E. Garcia, D. Brunner, B. LaBombard, and J. L. Terry, *J. Plasma Phys.* **86**, 905860519 (2020).
- <sup>29</sup>R. Kube, O. E. Garcia, A. Theodorsen, D. Brunner, A. Q. Kuang, B. LaBombard, and J. L. Terry, *Plasma Phys. Controlled Fusion* **60**, 065002 (2018).
- <sup>30</sup>R. Kube, A. Theodorsen, O. E. Garcia, B. LaBombard, and J. L. Terry, *Plasma Phys. Controlled Fusion* **58**, 054001 (2016).
- <sup>31</sup>A. Theodorsen, O. E. Garcia, J. Horacek, R. Kube, and R. A. Pitts, *Plasma Phys. Controlled Fusion* **58**, 044006 (2016).
- <sup>32</sup>F. A. C. Pereira, D. L. Toufen, Z. O. Guimarães-Filho, I. L. Caldas, R. L. Viana, and K. W. Gentle, *Phys. Plasmas* **28**, 032301 (2021).
- <sup>33</sup>Z. O. Guimarães-Filho, I. L. Caldas, R. L. Viana, J. Kurths, I. C. Nascimento, and Y. K. Kuznetsov, *Phys. Lett. A* **372**, 1088 (2008).
- <sup>34</sup>Z. O. Guimarães-Filho, G. Z. dos Santos Lima, I. L. Caldas, R. L. Viana, I. C. Nascimento, and Y. K. Kuznetsov, *J. Phys. Conf. Ser.* **246**, 012014 (2010).
- <sup>35</sup>R. L. Viana, D. L. Toufen, Z. O. Guimarães-Filho, I. L. Caldas, K. W. Gentle, and I. C. Nascimento, "Recurrence analysis of turbulent fluctuations in magnetically confined plasmas," in *Recurrence Plots and Their Quantifications: Expanding Horizons*, edited by C. L. Webber, Jr., C. Ioana, and N. Marwan (Springer International Publishing, 2016) pp. 341–353.
- <sup>36</sup>J.-P. Eckmann, S. O. Kamphorst, and D. Ruelle, *EPL* **4**, 973 (1987).
- <sup>37</sup>C. L. Webber and Z. J. P., *J. Appl. Physiol.* **76**, 965 (1994).
- <sup>38</sup>N. Marwan, N. Wessel, U. Meyerfeldt, A. Schirdewan, and J. Kurths, *Phys. Rev. E* **66**, 026702 (2002).
- <sup>39</sup>R. M. O. Galvão, C. H. S. Amador, W. A. H. Baquero, F. Borges, I. L. Caldas, N. A. M. Cuevas, V. N. Duarte, A. G. Elfimov, J. I. Elizondo, A. M. M. Fonseca, T. M. Germano, G. G. Grenfell, Z. O. Guimarães-Filho, J. L. Jeronimo, Y. K. Kuznetsov, M. A. M. Manrique, I. C. Nascimento, C. J. A. Pires, P. G. P. Puglia, A. P. Reis, G. Ronchi, L. F. Ruchko, W. P. de Sá, R. J. F. Sgalla, E. K. Sanada, J. H. F. Severo, V. C. Theodoro, and D. L. Toufen, *J. Phys.: Conf. Ser.* **591**, 012001 (2015).
- <sup>40</sup>G. G. Grenfell, I. C. Nascimento, D. S. Oliveira, Z. O. Guimarães-Filho, J. I. Elizondo, A. P. Reis, R. M. O. Galvão, W. A. H. Baquero, A. M. Oliveira, G. Ronchi, W. P. de Sá, and J. H. F. Severo, *Phys. Plasmas* **25**, 072301 (2018).
- <sup>41</sup>E. Parzen, *Stochastic Processes* (Society for Industrial and Applied Mathematics, 1999).
- <sup>42</sup>A. Gut, *Probability: A Graduate Course* (Springer-Verlag New York, 2013).
- <sup>43</sup>D. T. Gillespie, *Phys. Rev. E* **54**, 2084 (1996).
- <sup>44</sup>Z. Schuss, *Theory and Applications of Stochastic Processes* (Springer-Verlag New York, 2010).
- <sup>45</sup>G. E. Uhlenbeck and L. S. Ornstein, *Phys. Rev.* **36**, 823 (1930).
- <sup>46</sup>A. Feuerverger and R. A. Mureika, *Ann. Stat.* **5**, 88 (1977).
- <sup>47</sup>P. R. Bevington and D. K. Robinson, *Data reduction and error analysis for the physical sciences; 3rd ed.*, 3rd ed. (McGraw-Hill, 2003).
- <sup>48</sup>J. R. Taylor, *An Introduction to Error Analysis*, 2nd ed. (University Science Books, 1997).
- <sup>49</sup>S. F. Nørrelykke and H. Flyvbjerg, *Rev. Sci. Instrum.* **81**, 075103 (2010).
- <sup>50</sup>P. Welch, *IEEE Trans. on audio and electroacoustics* **15**, 70 (1967).
- <sup>51</sup>P. Podder, T. Z. Khan, M. H. Khan, and M. M. Rahman, *Int. J. Comput. Appl.* **96**, 1 (2014).
- <sup>52</sup>W. L. Briggs and V. E. Henson, *The DFT: An Owner's Manual for the Discrete Fourier Transform* (Society for Industrial and Applied Mathematics, 1995).
- <sup>53</sup>G. Y. Antar, S. I. Krasheninnikov, P. Devynck, R. P. Doerner, E. M. Hollmann, J. A. Boedo, S. C. Luckhardt, and R. W. Conn, *Phys. Rev. Lett.* **87**, 065001 (2001).
- <sup>54</sup>Y. H. Xu, S. Jachmich, R. R. Weynants, and the TEXTOR team, *Plasma Phys. Controlled Fusion* **47**, 1841–1855 (2005).
- <sup>55</sup>L. C. Appel, S. Kwak, F. Militello, and J. Svensson, *Plasma Phys. Controlled Fusion* **62**, 125002 (2020).
- <sup>56</sup>N. Kasdin, *Proc. IEEE* **83**, 802 (1995).
- <sup>57</sup>G. A. F. Seber and C. J. Wild, *Nonlinear Regression*, 2nd ed. (John Wiley & Sons, 2003).

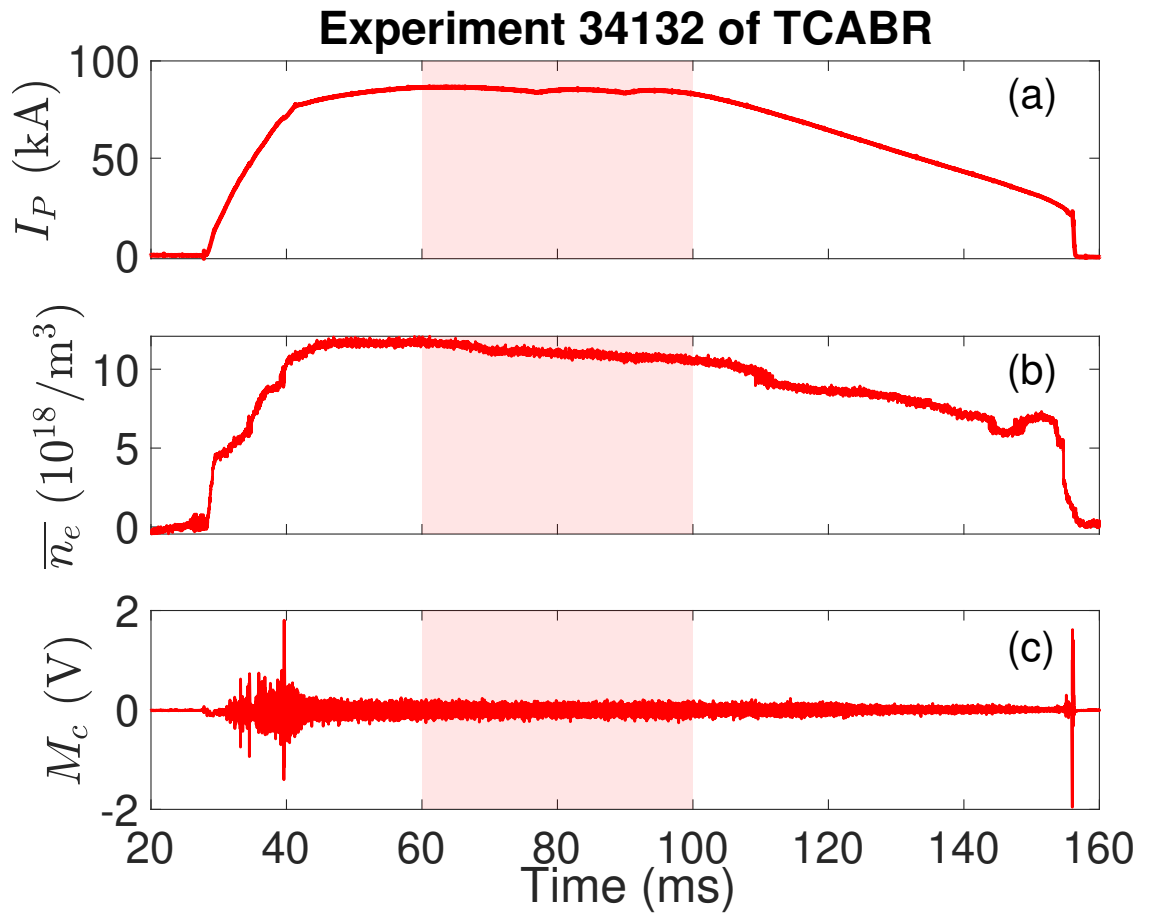
This is the author's peer reviewed, accepted manuscript. However, the online version of record will be different from this version once it has been copyedited and typeset.

PLEASE CITE THIS ARTICLE AS DOI: 10.1063/5.0081281



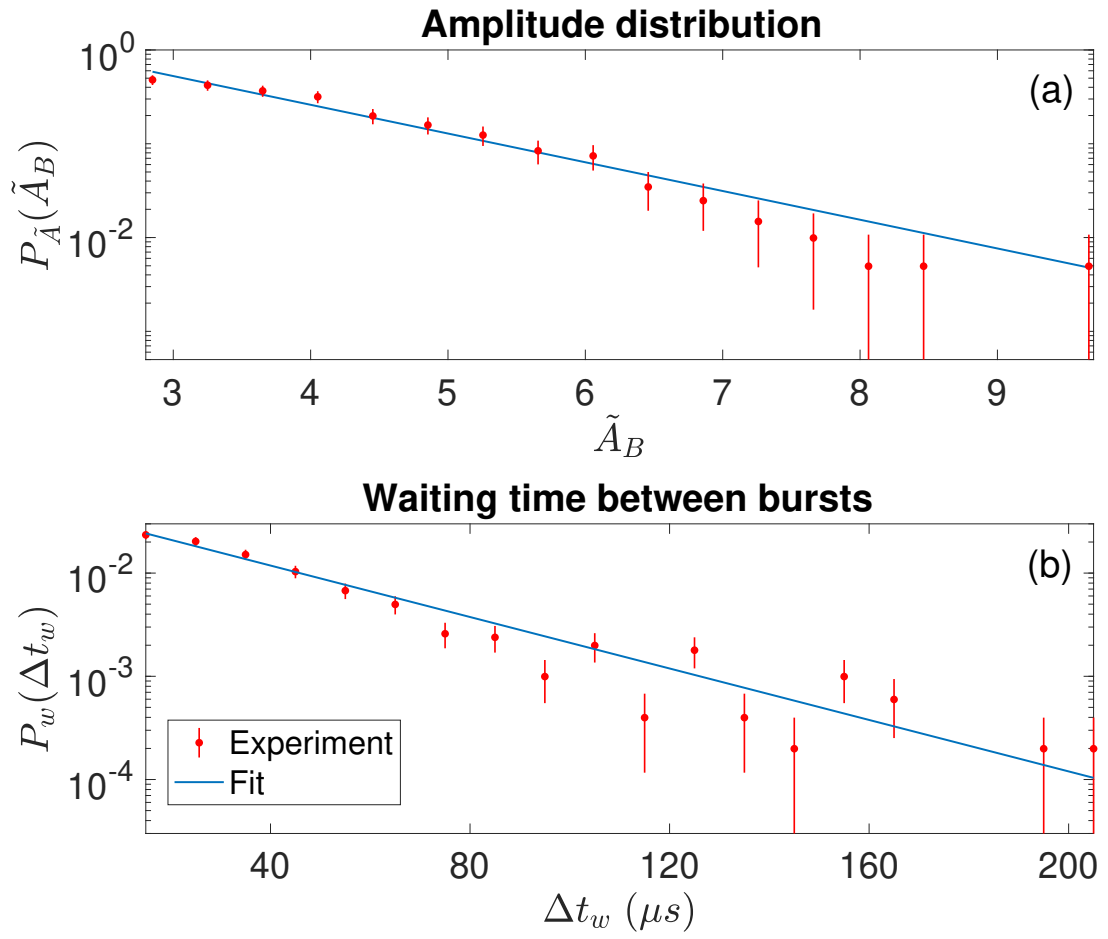
This is the author's peer reviewed, accepted manuscript. However, the online version of record will be different from this version once it has been copyedited and typeset.

PLEASE CITE THIS ARTICLE AS DOI: 10.1063/5.0081281



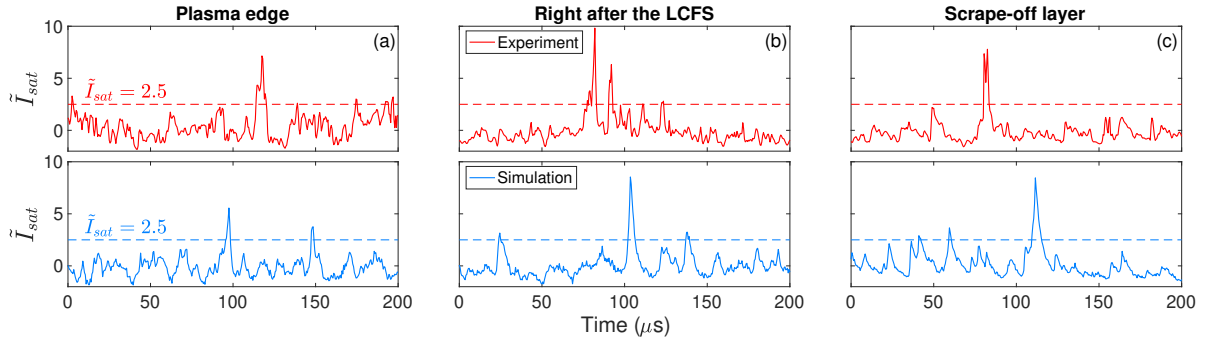
This is the author's peer reviewed, accepted manuscript. However, the online version of record will be different from this version once it has been copyedited and typeset.

PLEASE CITE THIS ARTICLE AS DOI: 10.1063/5.0081281



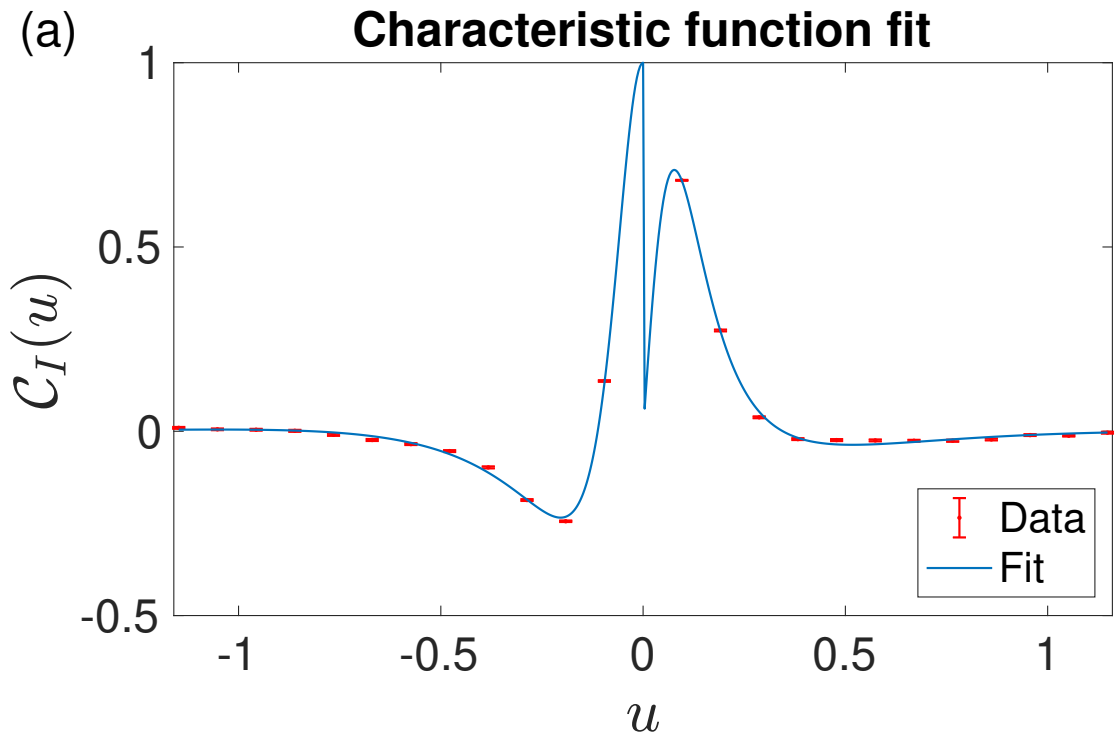
This is the author's peer reviewed, accepted manuscript. However, the online version of record will be different from this version once it has been copyedited and typeset.

PLEASE CITE THIS ARTICLE AS DOI: 10.1063/5.0081281



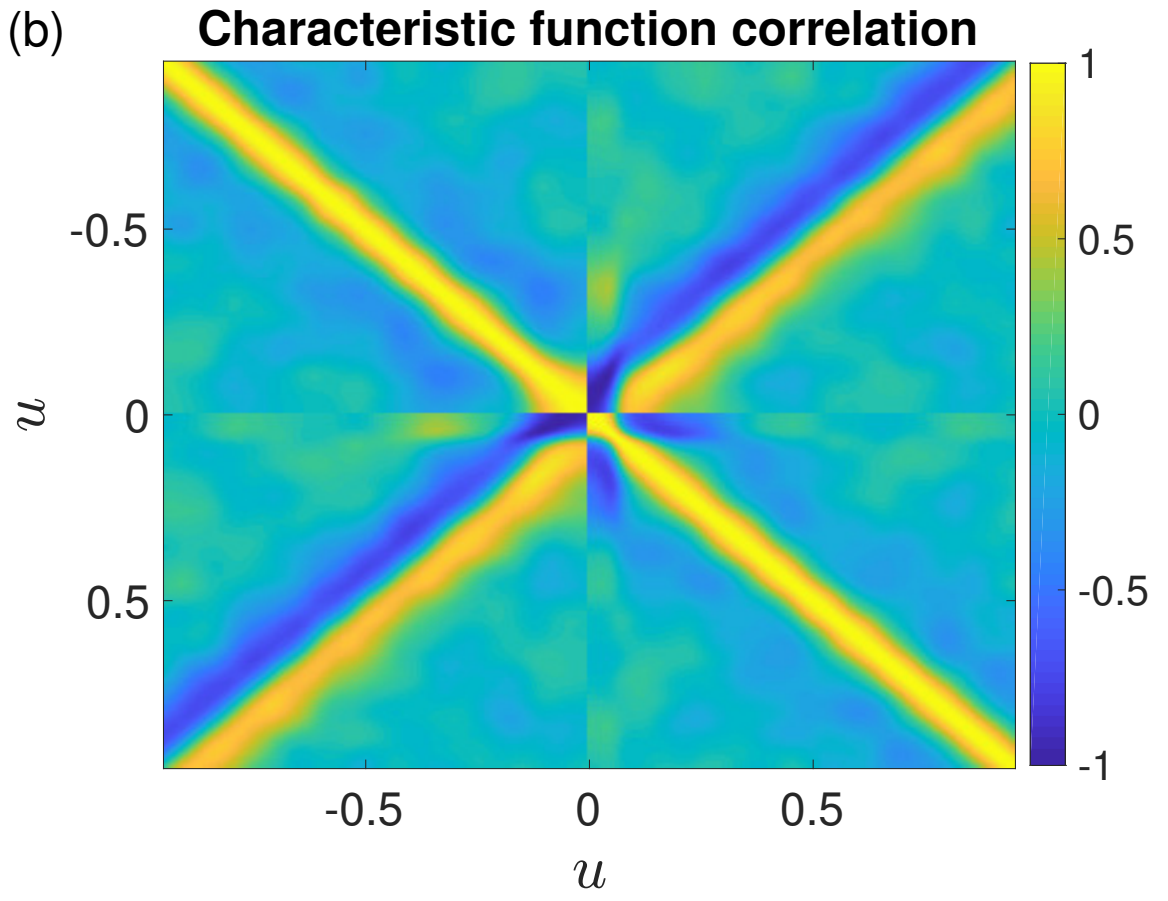
This is the author's peer reviewed, accepted manuscript. However, the online version of record will be different from this version once it has been copyedited and typeset.

PLEASE CITE THIS ARTICLE AS DOI: 10.1063/5.0081281



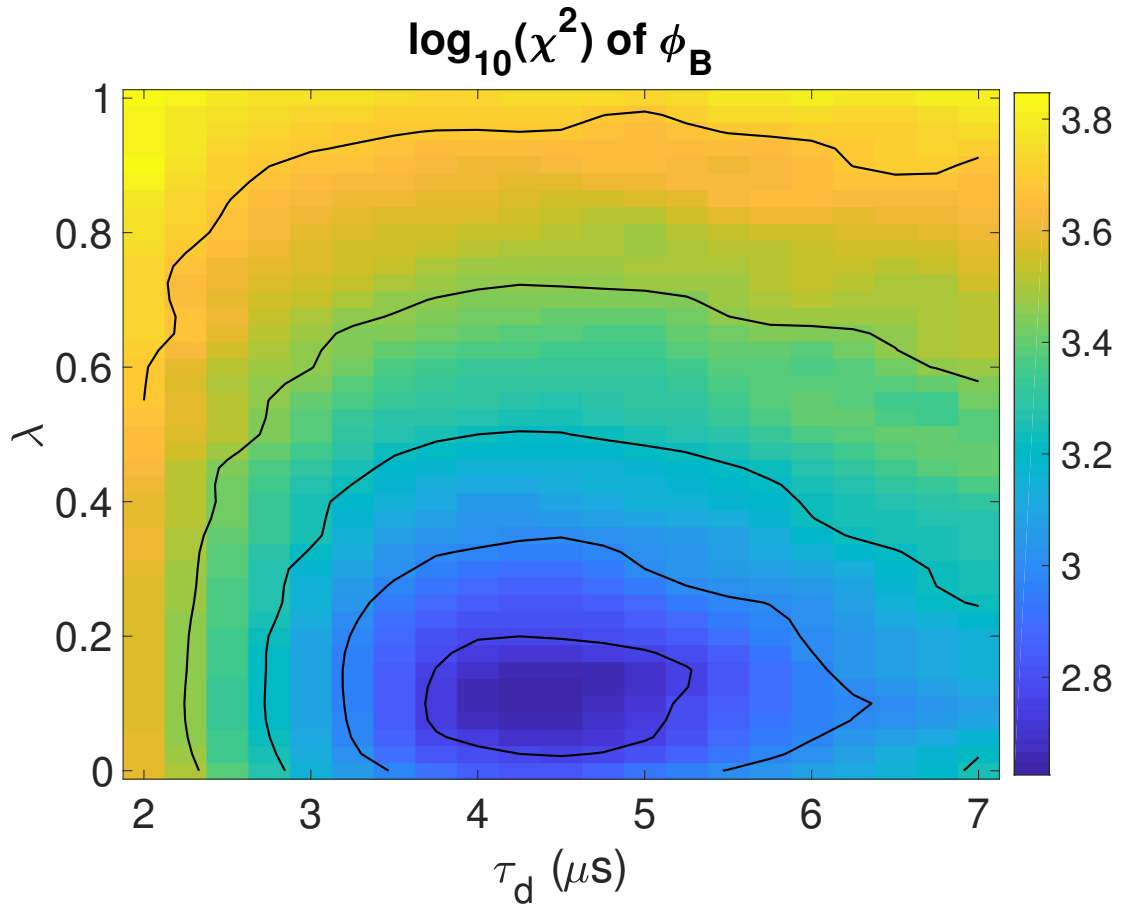
This is the author's peer reviewed, accepted manuscript. However, the online version of record will be different from this version once it has been copyedited and typeset.

PLEASE CITE THIS ARTICLE AS DOI: 10.1063/5.0081281



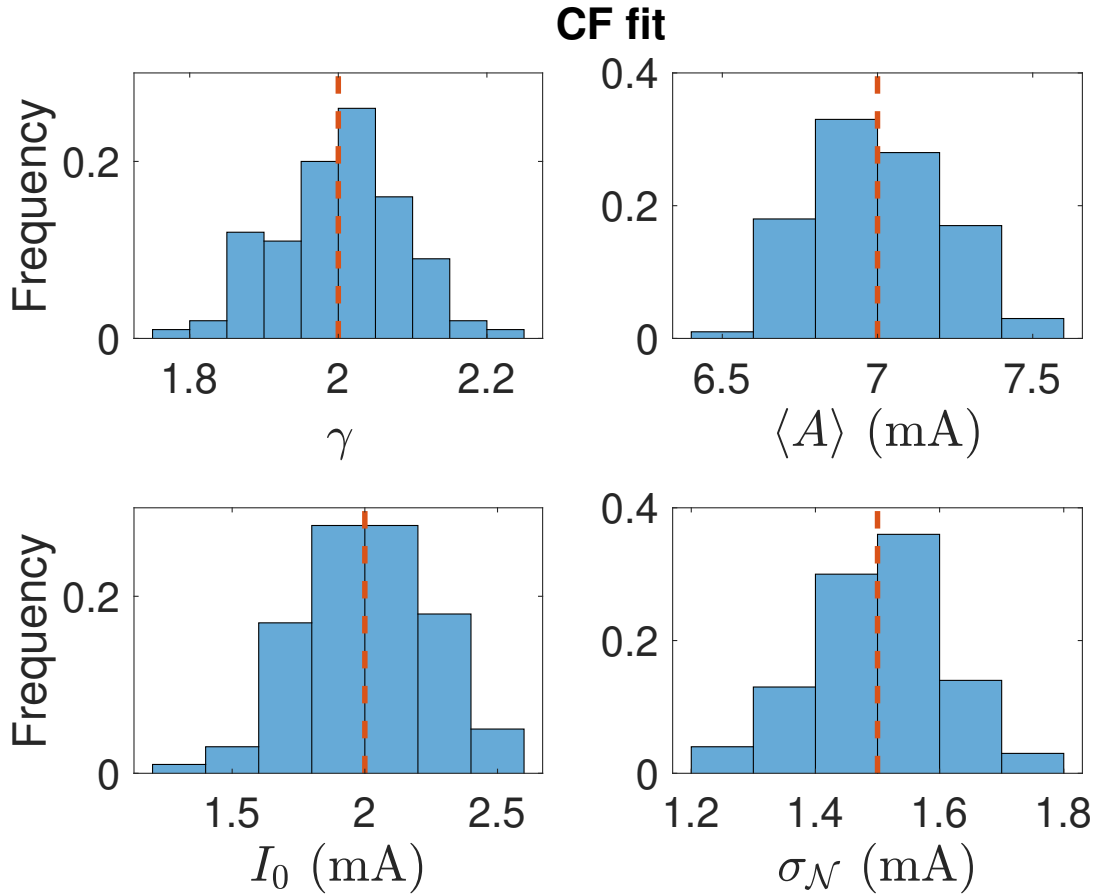
This is the author's peer reviewed, accepted manuscript. However, the online version of record will be different from this version once it has been copyedited and typeset.

PLEASE CITE THIS ARTICLE AS DOI: 10.1063/5.0081281



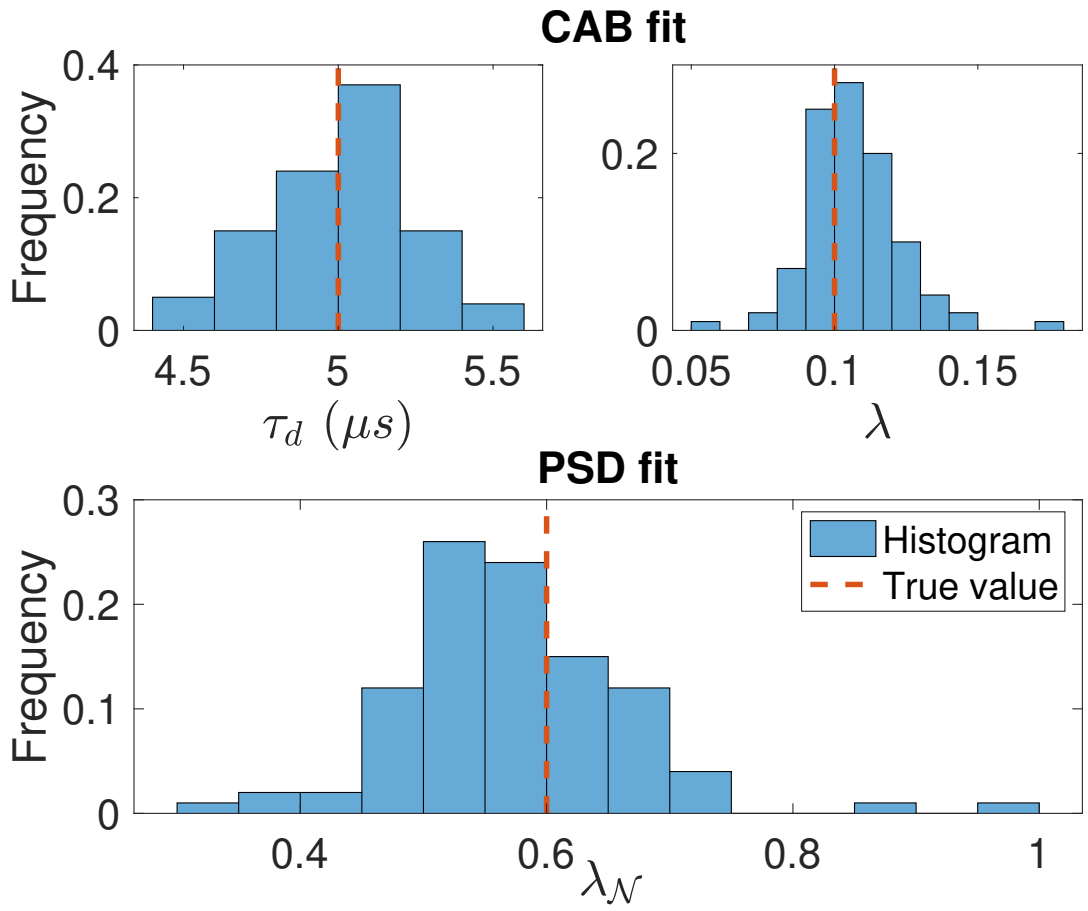
This is the author's peer reviewed, accepted manuscript. However, the online version of record will be different from this version once it has been copyedited and typeset.

PLEASE CITE THIS ARTICLE AS DOI: 10.1063/5.0081281



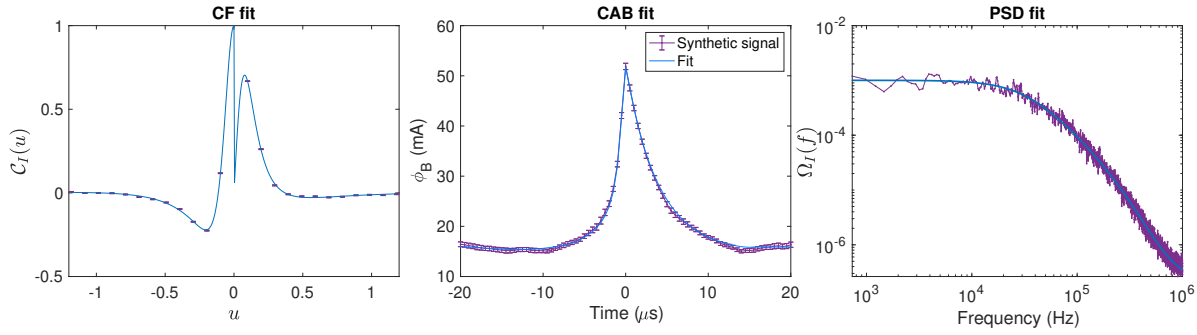
This is the author's peer reviewed, accepted manuscript. However, the online version of record will be different from this version once it has been copyedited and typeset.

PLEASE CITE THIS ARTICLE AS DOI: 10.1063/5.0081281

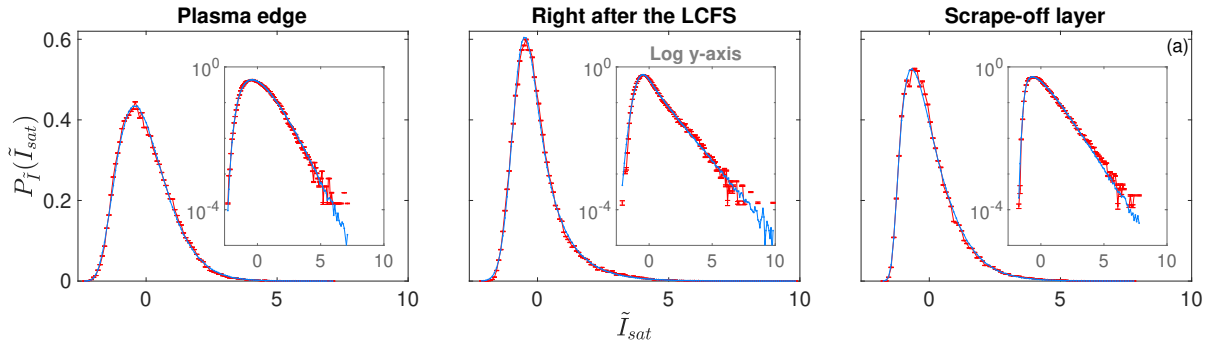


This is the author's peer reviewed, accepted manuscript. However, the online version of record will be different from this version once it has been copyedited and typeset.

PLEASE CITE THIS ARTICLE AS DOI: 10.1063/5.0081281

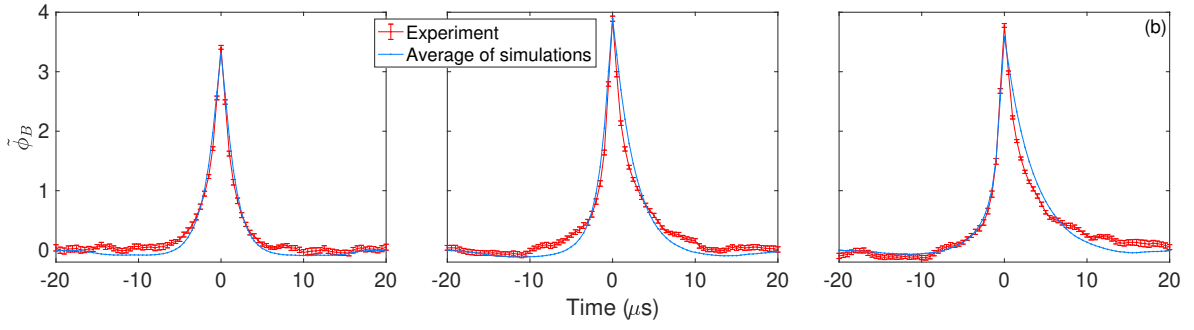


This is the author's peer reviewed, accepted manuscript. However, the online version of record will be different from this version once it has been copyedited and typeset.  
 PLEASE CITE THIS ARTICLE AS DOI: 10.1063/5.0081281



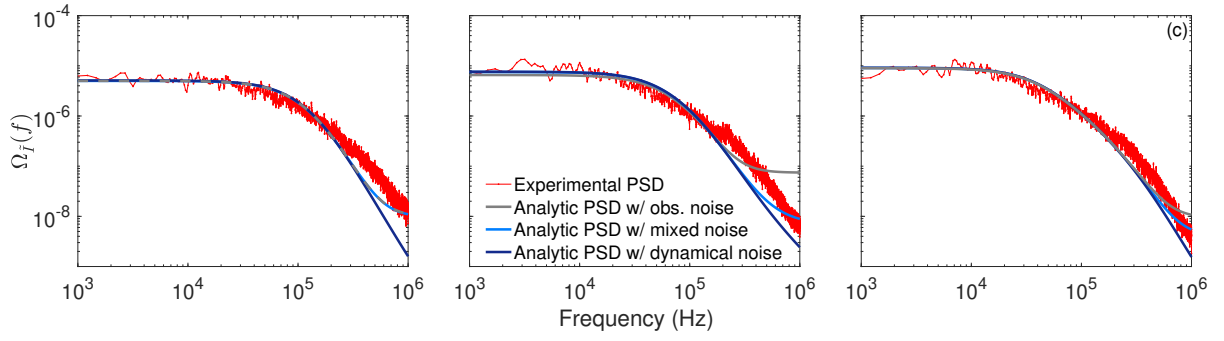
This is the author's peer reviewed, accepted manuscript. However, the online version of record will be different from this version once it has been copyedited and typeset.

PLEASE CITE THIS ARTICLE AS DOI: 10.1063/5.0081281

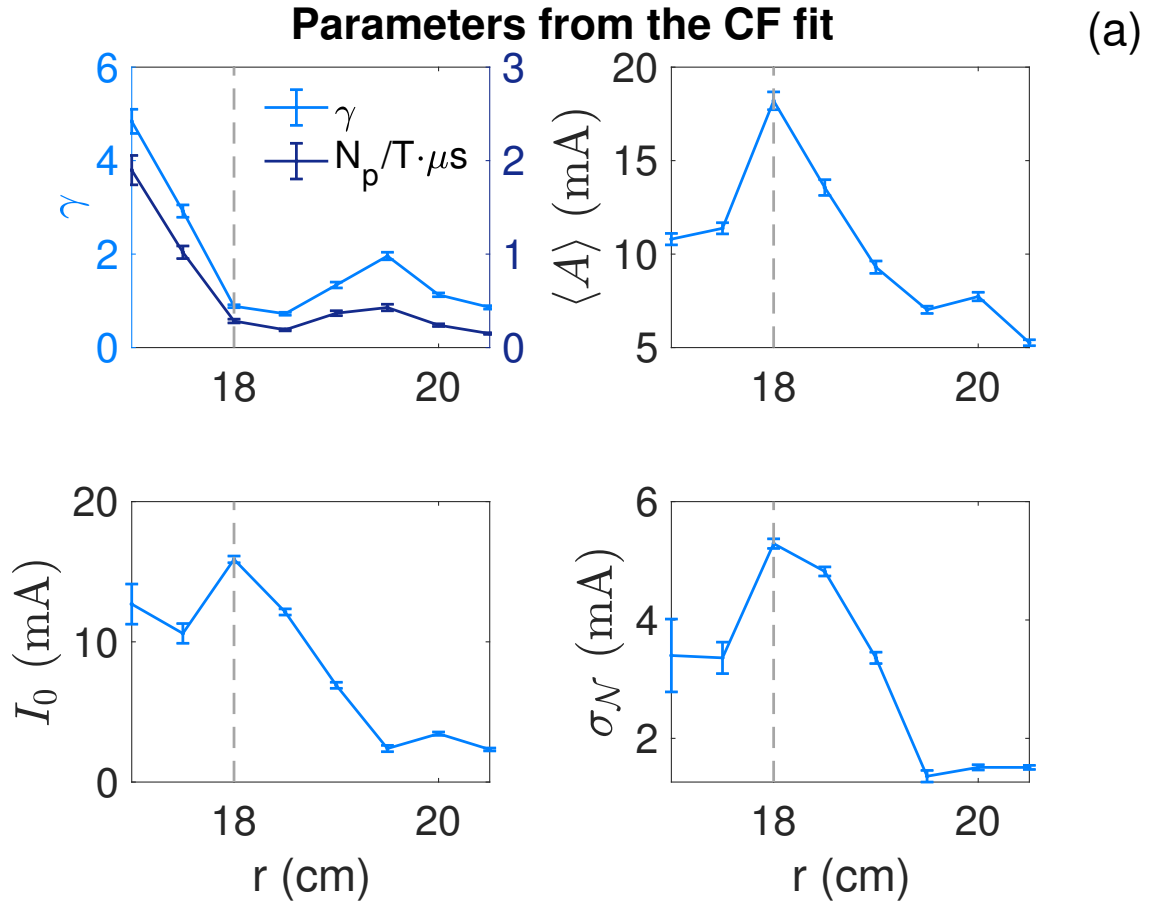


This is the author's peer reviewed, accepted manuscript. However, the online version of record will be different from this version once it has been copyedited and typeset.

PLEASE CITE THIS ARTICLE AS DOI: 10.1063/5.0081281

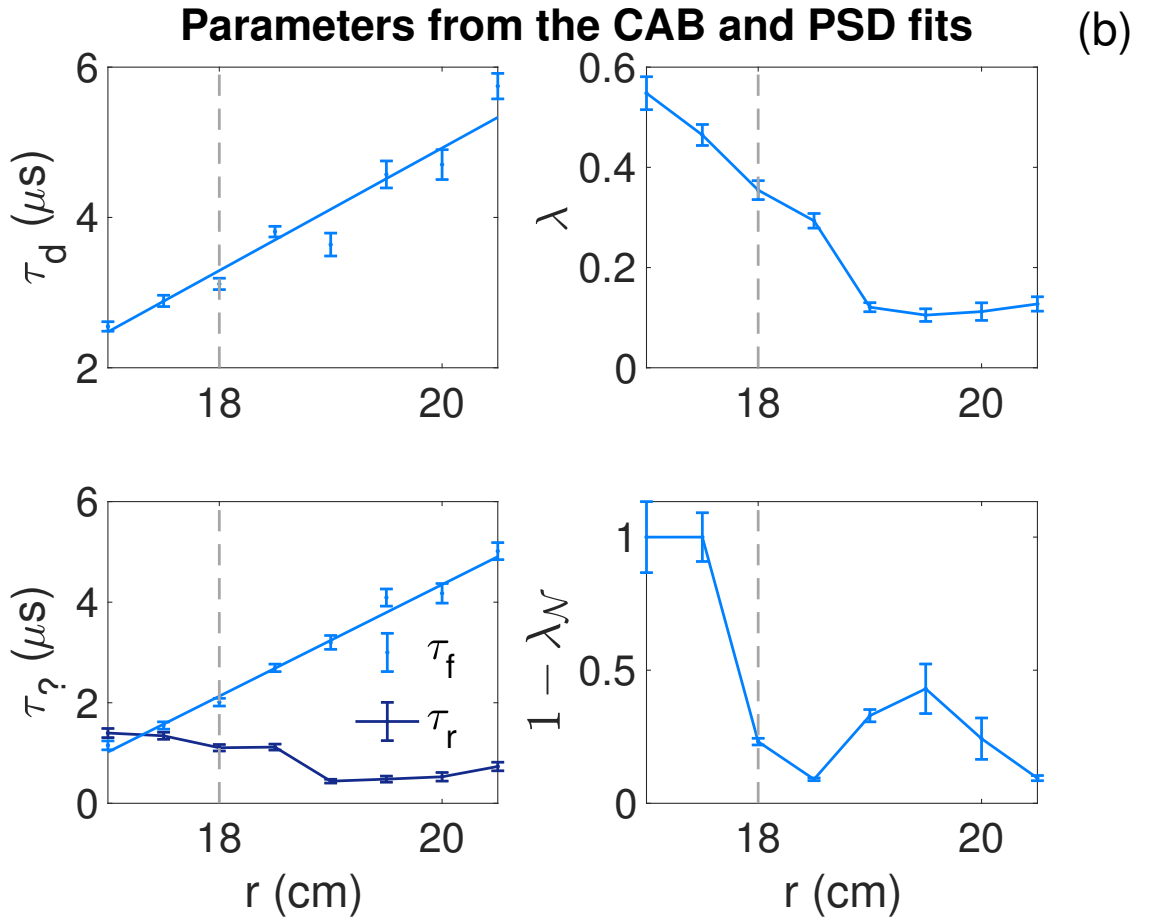


This is the author's peer reviewed, accepted manuscript. However, the online version of record will be different from this version once it has been copyedited and typeset.  
 PLEASE CITE THIS ARTICLE AS DOI: 10.1063/5.0081281



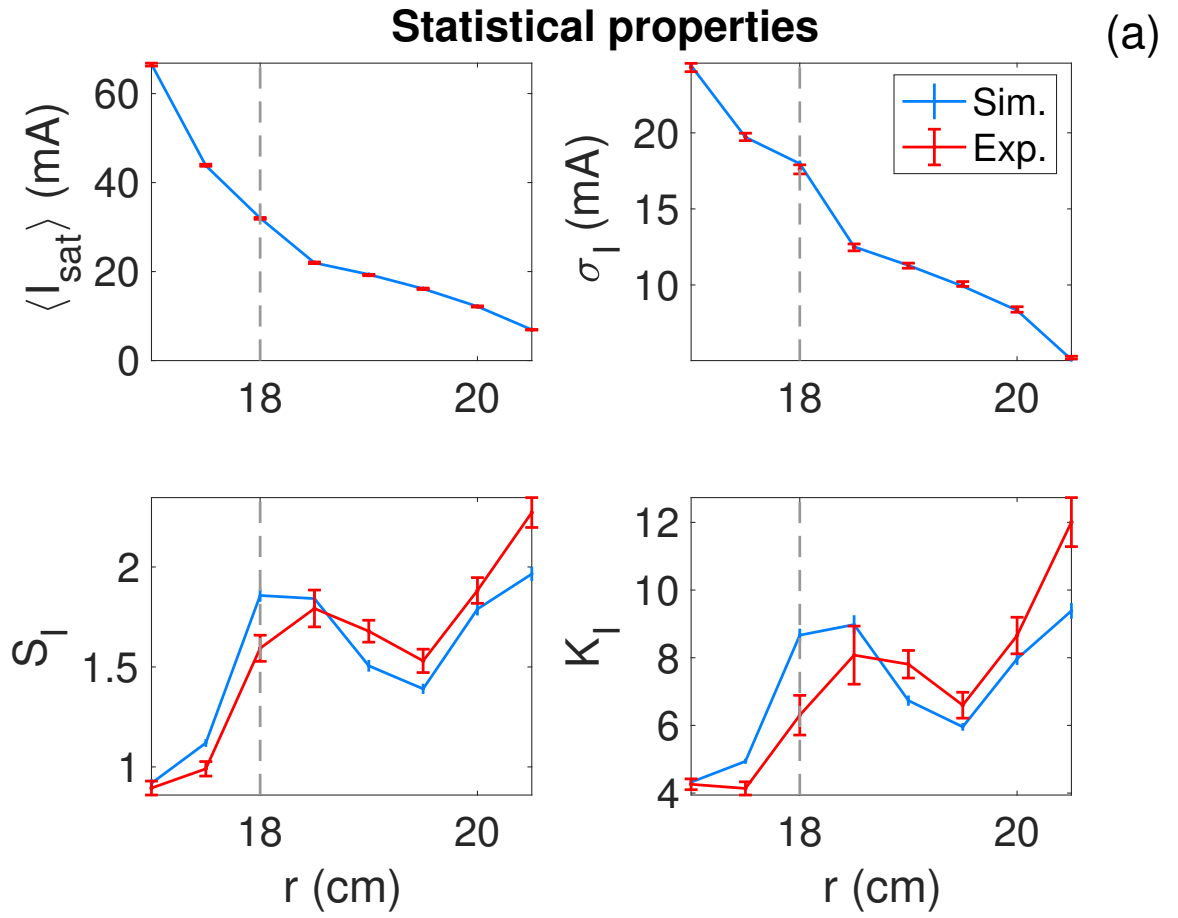
This is the author's peer reviewed, accepted manuscript. However, the online version of record will be different from this version once it has been copyedited and typeset.

PLEASE CITE THIS ARTICLE AS DOI: 10.1063/5.0081281



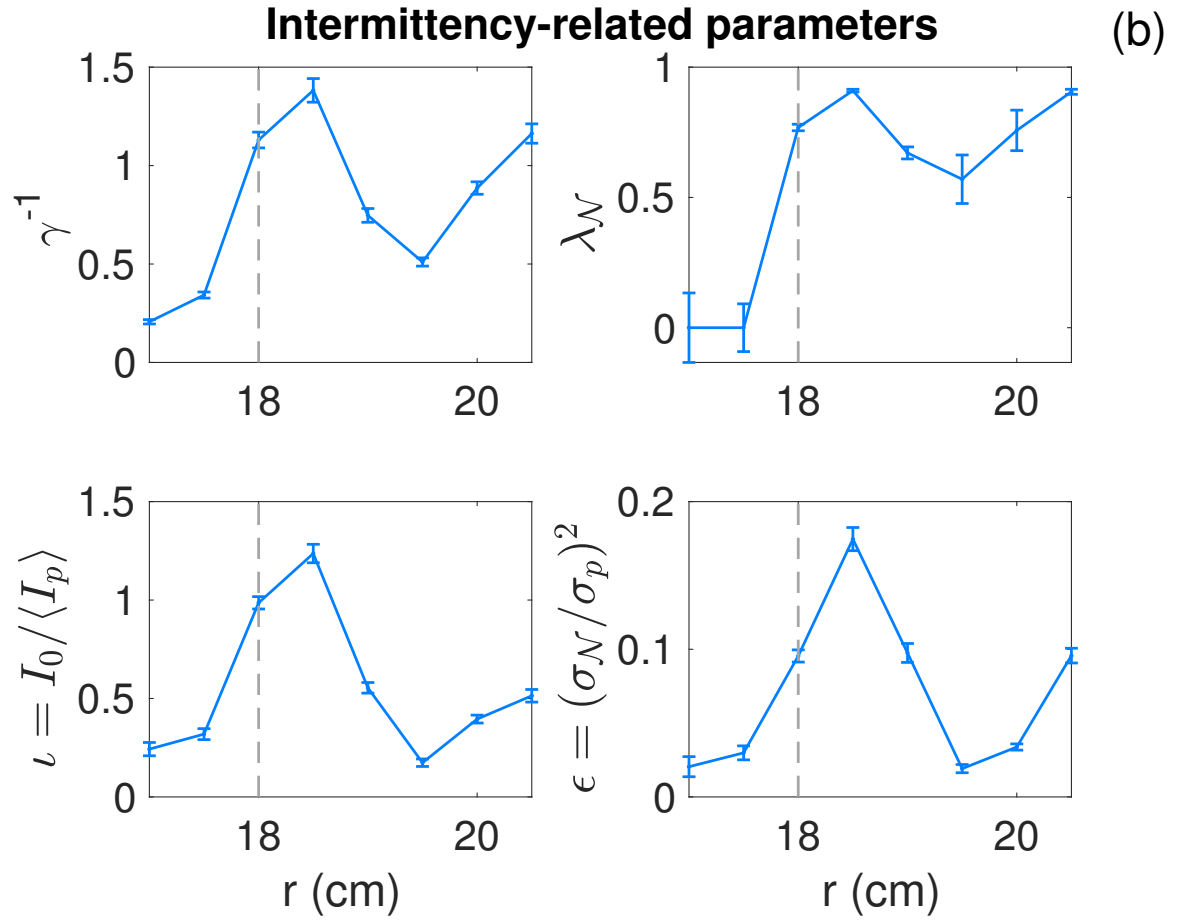
This is the author's peer reviewed, accepted manuscript. However, the online version of record will be different from this version once it has been copyedited and typeset.

PLEASE CITE THIS ARTICLE AS DOI: 10.1063/5.0081281



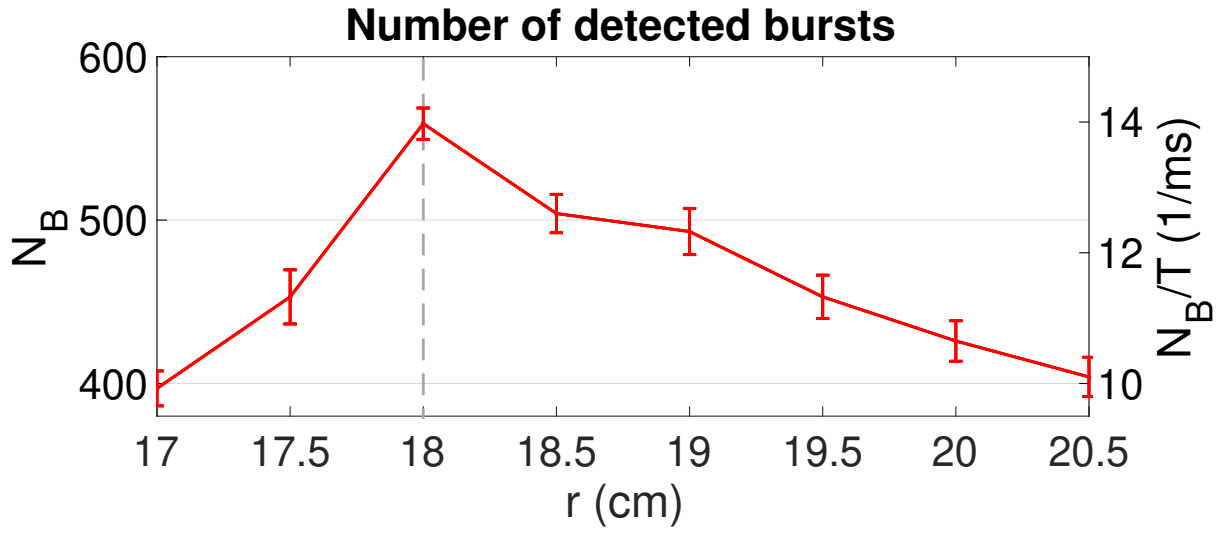
This is the author's peer reviewed, accepted manuscript. However, the online version of record will be different from this version once it has been copyedited and typeset.

PLEASE CITE THIS ARTICLE AS DOI: 10.1063/5.0081281



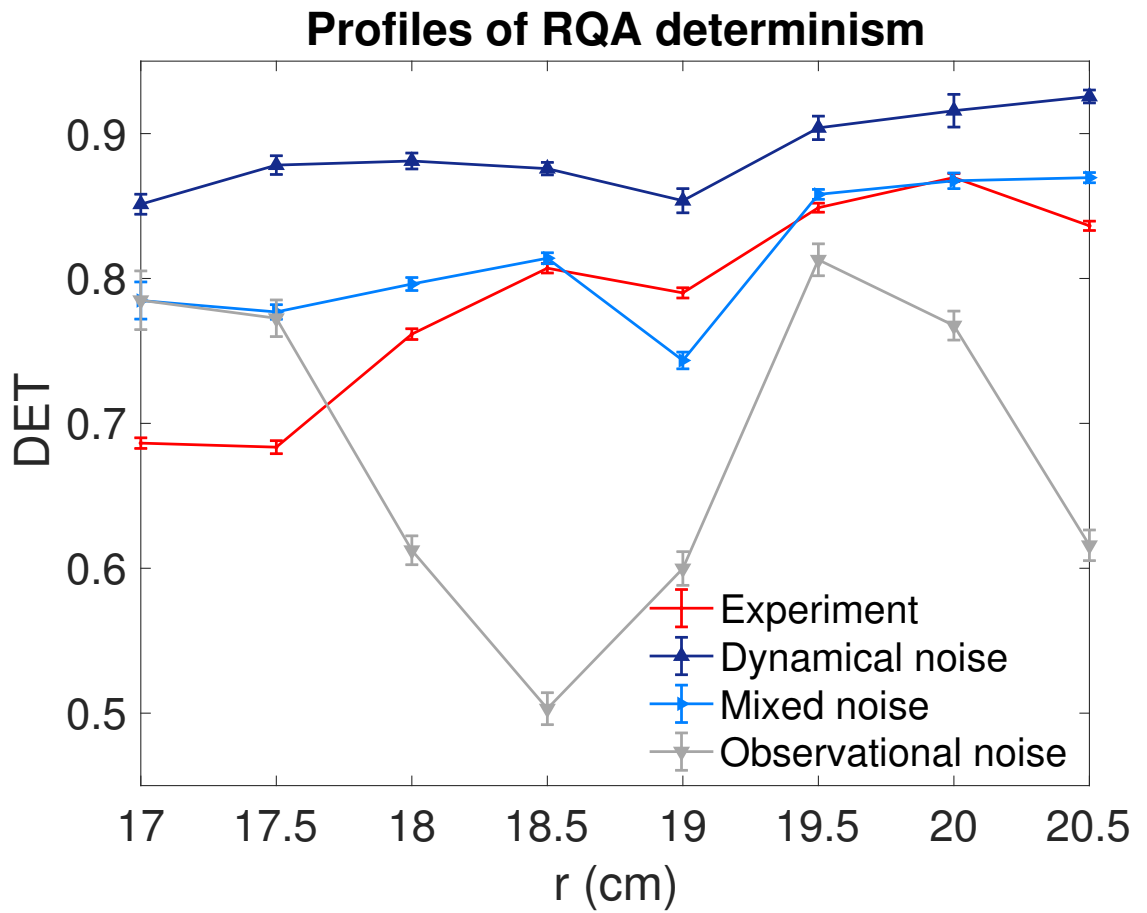
This is the author's peer reviewed, accepted manuscript. However, the online version of record will be different from this version once it has been copyedited and typeset.

PLEASE CITE THIS ARTICLE AS DOI: 10.1063/5.0081281



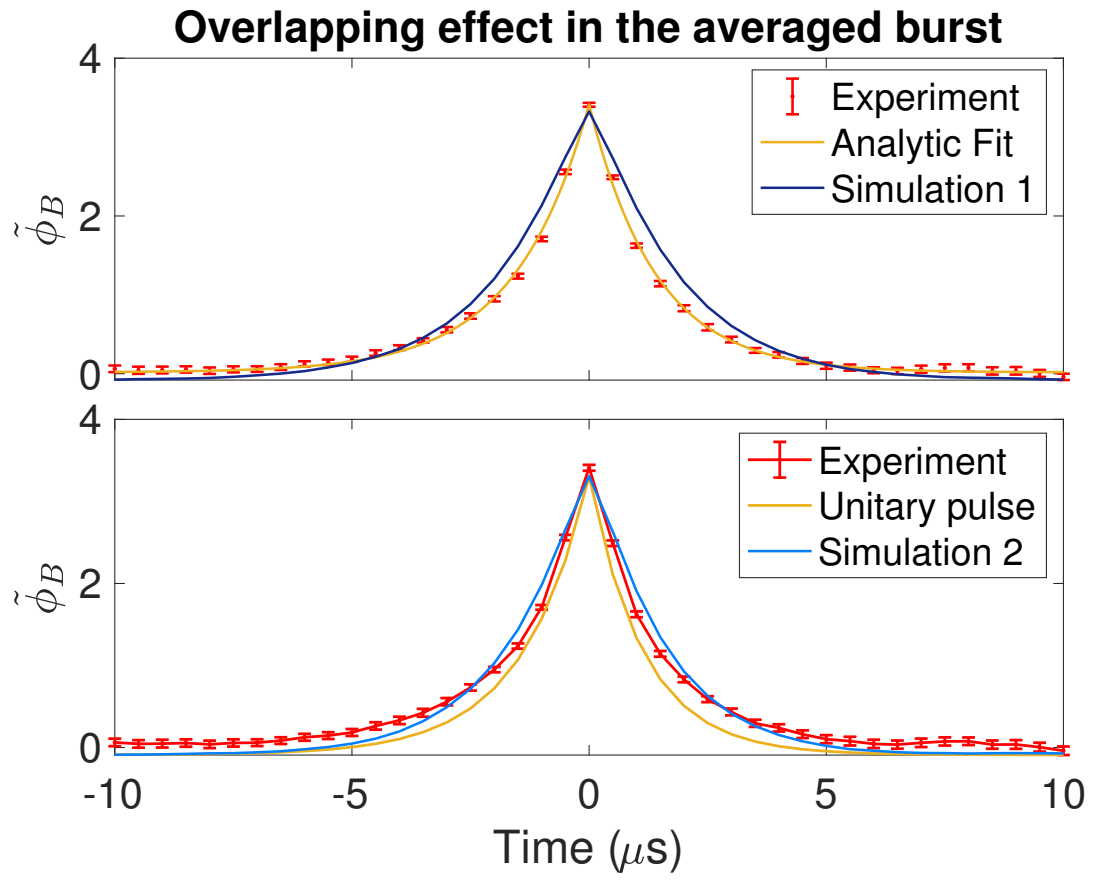
This is the author's peer reviewed, accepted manuscript. However, the online version of record will be different from this version once it has been copyedited and typeset.

PLEASE CITE THIS ARTICLE AS DOI: 10.1063/5.0081281



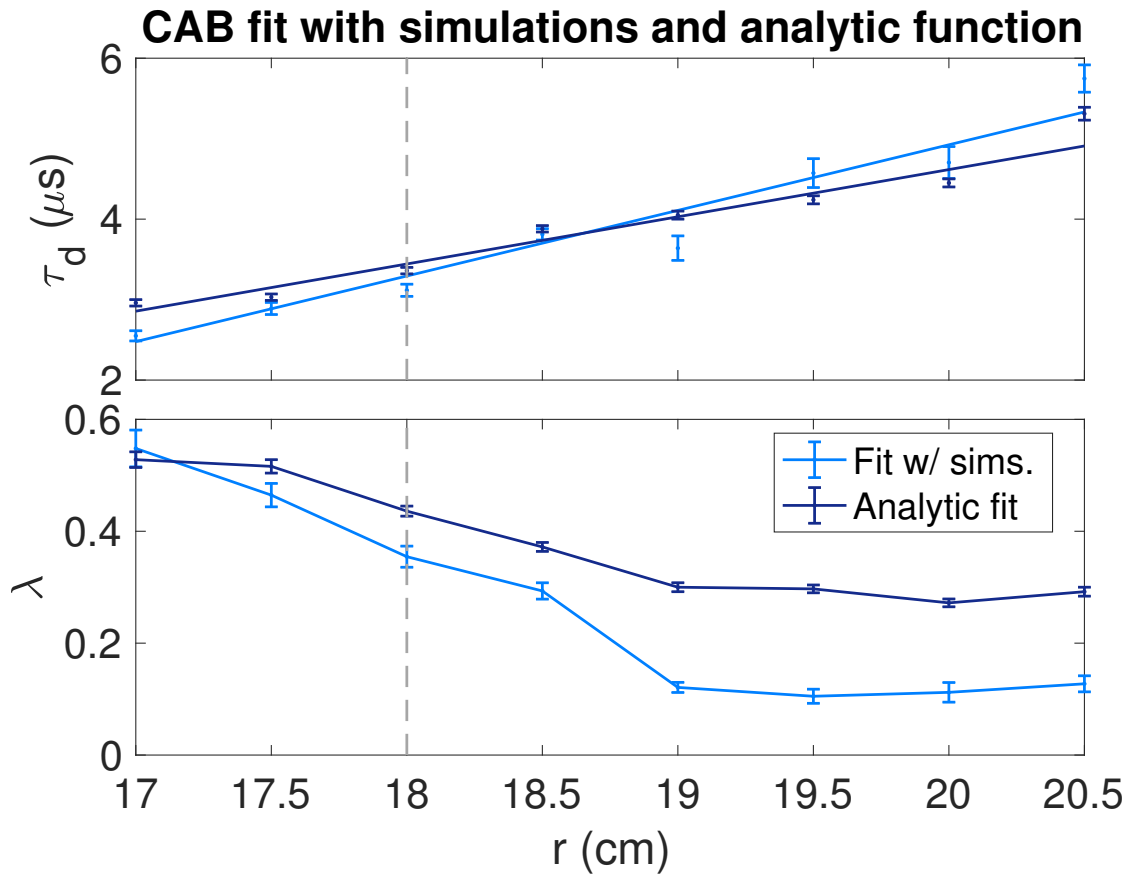
This is the author's peer reviewed, accepted manuscript. However, the online version of record will be different from this version once it has been copyedited and typeset.

PLEASE CITE THIS ARTICLE AS DOI: 10.1063/5.0081281



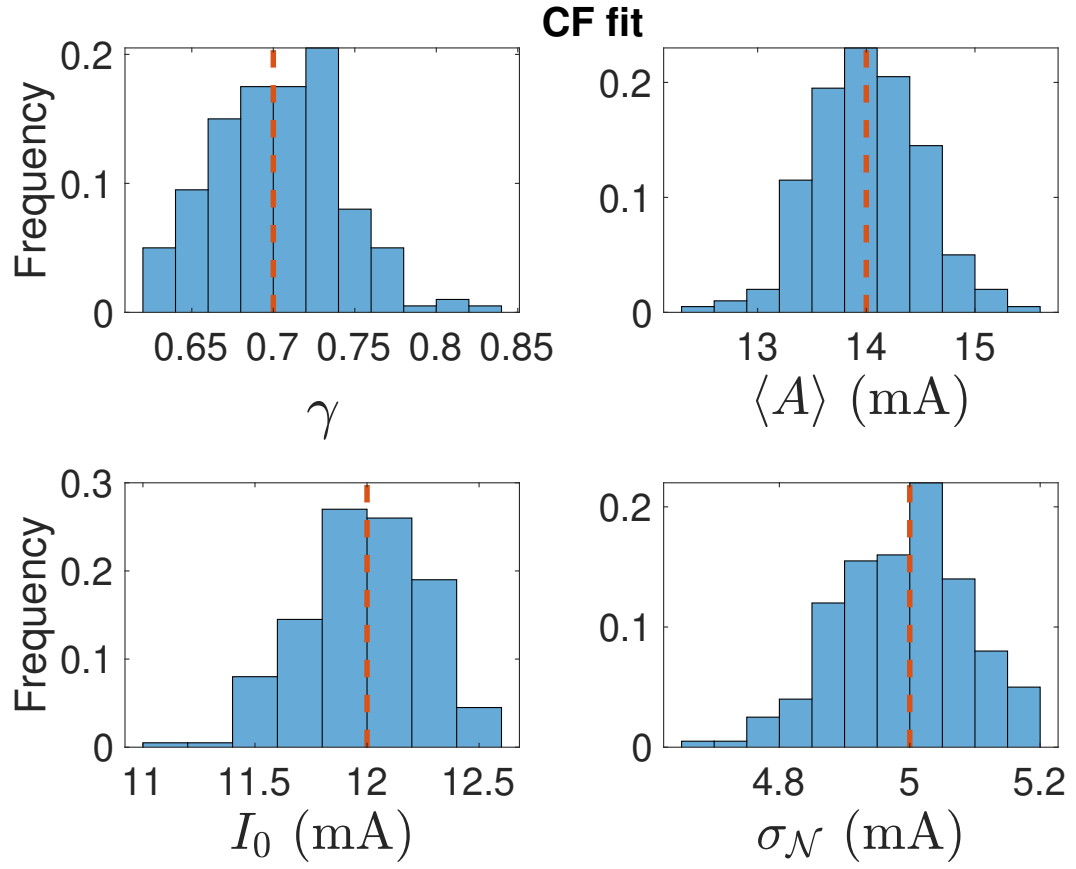
This is the author's peer reviewed, accepted manuscript. However, the online version of record will be different from this version once it has been copyedited and typeset.

PLEASE CITE THIS ARTICLE AS DOI: 10.1063/5.0081281



This is the author's peer reviewed, accepted manuscript. However, the online version of record will be different from this version once it has been copyedited and typeset.

PLEASE CITE THIS ARTICLE AS DOI: 10.1063/5.0081281



This is the author's peer reviewed, accepted manuscript. However, the online version of record will be different from this version once it has been copyedited and typeset.

PLEASE CITE THIS ARTICLE AS DOI: 10.1063/5.0081281

